A Survey of Atomic Carbon [C I] in High-redshift Main-Sequence Galaxies

Francesco Valentino, 1,2 Georgios E. Magdis, 1,2,3 Emanuele Daddi, Daizhong Liu, Manuel Aravena, 6 FRÂNCESCO VALENTINO, GEORGIOS E. MAGDIS, EMANUELE DADDI, DAIZHONG LIC, MANUEL ARAVENA,
FRÉDÉRIC BOURNAUD, ANNA CIBINEL, DIANE CORMIER, MARK E. DICKINSON, YU GAO, SHUOWEN JIN, 4,10
STÉPHANIE JUNEAU, JEYHAN KARTALTEPE, MIN-YOUNG LEE, ZUZANNE C. MADDEN, ANNAGRAZIA PUGLISI, DAVID SANDERS, AND JOHN SILVERMAN¹⁴

¹ Dawn Cosmic Center, Niels Bohr Institute, University of Copenhagen, Juliane Maries Vej 30, DK-2100 Copenhagen, Denmark ²Dark Cosmology Centre, Niels Bohr Institute, University of Copenhagen, Juliane Maries Vej 30, DK-2100 Copenhagen, Denmark ³ Institute for Astronomy, Astrophysics, Space Applications and Remote Sensing, National Observatory of Athens, GR-15236 Athens,

⁴Laboratoire AIM-Paris-Saclay, CEA/DSM-CNRS-Université Paris Diderot, Irfu/Service d'Astrophysique, CEA Saclay, Orme des Merisiers, F-91191 Gif sur Yvette, France

⁵Max Planck Institute for Astronomy, Königstuhl 17, D-69117 Heidelberg, Germany

⁶ Núcleo de Astronomía, Facultad de Ingeniería y Ciencias, Universidad Diego Portales, Av. Ejrcito 441, Santiago, Chile ⁷ Astronomy Centre, Department of Physics and Astronomy, University of Sussex, Brighton, BN1 9QH, UK

National Optical Astronomy Observatory, 950 North Cherry Avenue, Tucson, AZ 85719, USA

⁹Purple Mountain Observatory/Key Laboratory for Radio Astronomy, Chinese Academy of Sciences, 6 YuanHua Road, Nanjing 210034. People's Republic of China

¹⁰School of Astronomy and Space Science, Nanjing University, Nanjing 210093, China ¹¹School of Physics and Astronomy, Rochester Institute of Technology, 84 Lomb Memorial Drive, Rochester NY 14623, USA ¹² Max-Planck-Institut fr Radioastronomie, Auf dem Hgel 69, D-53121 Bonn, Germany

¹³ University of Hawaii, Institute for Astronomy, 2680 Woodlawn Drive, Honolulu, HI, 96822, USA

¹⁴Kavli Institute for the Physics and Mathematics of the Universe, Todai Institutes for Advanced Study, the University of Tokyo, Kashiwa, Japan 277-8583 (Kavli IPMU, WPI)

(Received 2018; Revised 2018)

Submitted to ApJ

ABSTRACT

We present the first results of an ALMA survey of the lower fine structure line of atomic carbon $[CI](^3P_1 - {}^3P_0)$ in far infrared-selected galaxies on the main sequence at $z \sim 1.2$ in the COSMOS field. We compare our sample with a comprehensive compilation of data available in literature for local and high-redshift starbursting systems and quasars. We show that the $[CI](^3P_1 \rightarrow ^3P_0)$ luminosity correlates on global scales with the infrared luminosity $L_{\rm IR}$ similarly to low-J CO transitions. We report a systematic variation of $L'_{[C\,1]^3P_1\,-\,^3P_0}/L_{\rm IR}$ as a function of the galaxy type, with the ratio being larger for main-sequence galaxies than for starbursts and sub-millimeter galaxies at fixed $L_{\rm IR}$. The $L'_{[C_I]^3P_1={}^3P_0}/L'_{CO(2-1)}$ and $M_{[C_I]}/M_{dust}$ mass ratios are similar for main-sequence galaxies and for local and high-redshift starbursts within a 0.2 dex intrinsic scatter, suggesting that [C I] is a good tracer of molecular gas mass as CO and dust. We derive a fraction of $f_{\rm [C\,I]}=M_{\rm [C\,I]}/M_{\rm C}\sim 3-13\%$ of the total carbon mass in the atomic neutral phase. Moreover, we estimate the neutral atomic carbon abundance, the fundamental ingredient to calibrate [CI] as a gas tracer, by comparing $L'_{[CI]^3P_1-{}^3P_0}$ and available gas masses from CO lines and dust emission. We find lower [CI] abundances in mainsequence galaxies than in starbursting systems and sub-millimeter galaxies, as a consequence of the canonical $\alpha_{\rm CO}$ and gas-to-dust conversion factors. This argues against the application to different galaxy populations of a universal standard [CI] abundance derived from highly biased samples.

Corresponding author: Francesco Valentino francesco.valentino@nbi.ku.dk

Keywords: Galaxies: evolution, ISM, star formation, high-redshift — Submillimeter: galaxies, ISM

1. INTRODUCTION

The growth, structure, dynamics, and eventually fate of star-forming galaxies is largely regulated by the amount of gas available to form stars, therefore a crucial parameter to estimate. While low-J transitions of carbon monoxide ¹²CO molecules and optically thin dust emission are generally trustable tracers for the molecular gas content of galaxies, they depend on the excitation conditions, metallicity, radiation field, redshift, geometry, or a good photometric coverage of the far-infrared emission, and their applicability becomes progressively more observing time consuming with increasing redshift (e.g., Magdis et al. 2012a, 2017; Carilli & Walter 2013; Bolatto et al. 2013; Scoville et al. 2014). Alternative and independent proxies are, therefore, highly valuable. These include cold molecular and photodissociation region (PDR) gas tracers, responsible for a large fraction of cooling (e.g., [C II] $\lambda 158 \mu m$, Zanella et al. 2018; polycyclic aromatic hydrocarbon features, PAHs, Cortzen et al. 2018).

The sub-millimetric atomic carbon transitions [CI] $({}^{3}P_{1} \rightarrow {}^{3}P_{0}) \ (\nu_{\text{rest}} = 492.161 \text{ GHz}) \text{ and } [\text{C I}] \ ({}^{3}P_{2} \rightarrow {}^{3}P_{1})$ $(\nu_{\rm rest} = 809.344 \text{ GHz})$ have been put forward as potential tracers of the bulk of the molecular gas in galaxies. These lines have an excitation temperature of $T_{\rm ex} = 23.6$ K and 62.5 K, respectively, and a critical density for collisions with hydrogen atoms of $n_{\rm crit} \approx 10^3 {\rm cm}^{-3}$. They can, thus, probe a wide range of ISM conditions, and they are normally found associated with PDRs. Early simple plane-parallel modeling of these regions, predicting [CI] just in narrow gas slabs between CO and [CII], generated an initial skepticism on the real usefulness of [CI] transitions as molecular gas tracers, recently overcome by a growing body of theoretical and observational work. Modern PDR models including non-equilibrium chemistry (Stoerzer et al. 1997), turbulent mixing (Xie et al. 1995; Glover et al. 2015), clumpy geometries (Stutzki et al. 1998), and the effect of cosmic rays (Papadopoulos et al. 2004; Bisbas et al. 2015, 2017) can better explain the detection of [C I] fully concomitant with CO (1-0) and ¹³CO over a wide range of conditions, with a surprisingly constant ratio $N([CI])/N(CO) \sim 0.1 - 0.2$ and tightly correlated intensities (e.g., Keene et al. 1996; Ojha et al. 2001; Ikeda et al. 2002).

The use of [CI] as a tracer of the molecular gas mass could be even advantageous over the traditional ¹²CO

molecule in many respects: (1) the [CI] lines are as optically thin as ^{13}CO ($\tau_{[C_I]} \sim 0.1 - 1$, Ojha et al. 2001; Ikeda et al. 2002 in giant molecular clouds in the Milky Way and its center), allowing us to probe higher column densities of cold molecular gas than ¹²CO; (2) they do not suffer from the "excitation bias" affecting the high-J ($J_{\rm up} \geq 4$) ¹²CO transitions, the latter being unable to capture cool (kinetic temperature $T_{\rm kin}$ < 50 K) and sub-thermally excited gas (at densities of $n < 10^4$ cm⁻³, Papadopoulos et al. 2004), especially in presence of strong UV radiation fields; (3) models show that the $[CI](^3P_1 - ^3P_0)$ luminosity correlates with the total $M_{\rm gas}$ better than both ionized carbon [C II] and CO (1-0), regardless of the local radiation intensity field and spanning at least 4 orders of magnitude in density $(n = 10 - 10^4 \text{ cm}^{-3}, \text{ Madden et al. in prep.}); (4)$ for the high cosmic rays rates expected in high-redshift galaxies, CO is destroyed, while [CI] and [CII] become more abundant (Papadopoulos et al. 2004; Bisbas et al. 2015, 2017); (5) the simple three-level structure of [CI] allows for breaking the temperature-density degeneracy hampering other line tracers, and the excitation conditions of the molecular gas (i.e., its excitation temperature $T_{\rm ex}$) can be straightforwardly derived from the ratio $L'_{[C_1]^3P_2-{}^3P_1}/L'_{[C_1]^3P_1-{}^3P_0}$ (Weiß et al. 2003).

The $[CI](^3P_1 - ^3P_0)$ and $[CI](^3P_2 - ^3P_1)$ transitions have been detected in molecular clouds of the Galactic disk, the Galactic center, and other nearby galaxies (Stutzki et al. 1997; Gerin & Phillips 2000; Ojha et al. 2001; Ikeda et al. 2002 for some early measurements, Kamenetzky et al. 2016; Israel et al. 2015; Lu et al. 2017; Jiao et al. 2017 among the others for more recent compilations). At high redshift, the detections reported so far include strongly starbursting sub-millimeter galaxies (SMGs), radio-galaxies, and quasar hosts (QSOs), often gravitationally lensed and magnified up to factor of 30× (e.g., Walter et al. 2011; Alaghband-Zadeh et al. 2013; Gullberg et al. 2016; Bothwell et al. 2017; Popping et al. 2017, and references therein). First results seem to indicate that in these galaxies the excitation properties of the interstellar medium and the [CI] abundances are similar or more extreme than in (Ultra-)Luminous InfraRed Galaxies ((U)LIRGs) and starbursts in the local Universe. Nevertheless, despite being a valuable reference sample, this handful of galaxies (~ 35) selected in diverse ways is not representative of the average mainsequence population (e.g., Noeske et al. 2007; Daddi et al. 2007; Elbaz et al. 2007; Magdis et al. 2010), thus strongly biasing the general conclusions we can draw about the bulk of high-redshift galaxies. In order to remedy this situation, we designed and carried out a survey with the Atacama Large Millimeter Array (ALMA), targeting $[CI](^3P_1 - ^3P_0)$ in upper mainsequence galaxies in the COSMOS field at $z \sim 1.2$. Here we present the first results on a sample of objects with secure $[CI](^3P_1 - ^3P_0)$, dust continuum, and/or CO(2-1) determinations, starting exploring the potential use of $[CI](^3P_1 - ^3P_0)$ as an effective tracer of the molecular gas on global scales in normal main-sequence galaxies.

This work is structured as follows. In Section 2 we describe how we selected the sample of main-sequence galaxies and the available data; in particular, in Section 2.3 we present the new ALMA data targeting $[CI](^3P_1 - ^3P_0)$, along with results from independent programs targeting other CO lines for the same objects; in Section 3 we compile data from the literature to build a comparison sample for our sources; Section 4 contains the analysis and the main results of this work, followed by a discussion in Section 5 and the conclusions in Section 6. Unless stated otherwise, we assume a Λ CDM cosmology with $\Omega_{\rm m}=0.3,\,\Omega_{\Lambda}=0.7,\,{\rm and}\,\,H_0=70~{\rm km}$ s⁻¹ Mpc⁻¹ and a Chabrier initial mass function (IMF, Chabrier 2003). All magnitudes are expressed in the AB system. All the literature data have been homogenized with our conventions.

2. SAMPLE AND OBSERVATIONS

2.1. Sample selection

We selected targets in the COSMOS field (Scoville et al. 2007) with (1) an available stellar mass estimate (Muzzin et al. 2013; Laigle et al. 2016); (2) a spectroscopic confirmation with optical or near-infrared spectrographs from the COSMOS master catalog (Salvato et al., in prep.); and (3) a Herschel/PACS 100 and/or $160 \ \mu \text{m} > 3\sigma$ detection in the publicly available PEP catalog (Lutz et al. 2011). The latter requirement resulted in the selection of massive galaxies mainly on the upper main sequence and with mean dust temperatures of $T_{\rm dust} \gtrsim 30$ K. We further chose sources at $z_{\rm opt/NIR} = 1.05 - 1.63$ to maximize the overlap with parallel and independent ALMA programs targeting CO(2-1) and CO(5-4) (Section 2.3, Daddi et al. in prep.). These criteria drove to an initial pool of 204 sources. We then grouped the sources to maximize the number of targets observable in 3 frequency configurations of ALMA Band 6. This resulted in the final selection of 50 sources in the redshift ranges $z_{\rm opt/NIR} = 1.09 - 1.18$ and 1.23 - 1.32, randomly sam-

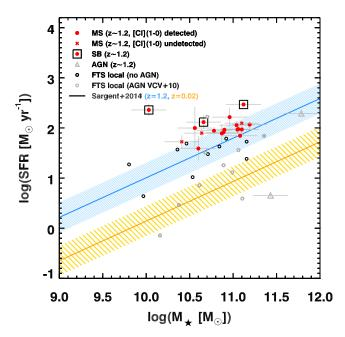


Figure 1. Stellar mass - SFR plane. Red filled circles and crosses mark our sample of MS galaxies at $z \sim 1.2$ with and without a $> 3\sigma$ [C I]($^3P_1 - ^3P_0$) detection, respectively. Black squares indicate starbursts. Gray triangles mark the position of the two AGN dominated galaxy in our sample. Open black and gray circles represent the local comparison sample of [C I]($^3P_1 - ^3P_0$)-detected LIRGs and active galaxies, respectively (Liu et al. 2015). The blue (orange) solid line and hatched area mark the position of the main sequence at z = 1.2 (z = 0.02) as parametrized by Sargent et al. (2014) and its 1σ scatter of 0.3 dex.

pling the whole interval of total infrared luminosities of the original parent sample. The first redshift interval allowed us to simultaneously cover [C I]($^3P_1 - ^3P_0$) and the CO (4 - 3) transition ($\nu_{\rm rest} = 461.041$ GHz, Section 2.3).

Here we present the results for 21 sources with both (1) an unambiguous spectroscopic confirmation from a sub-millimeter transition, and (2) an estimate of the CO(2-1) flux and/or of the dust continuum emission, so to ensure at least one molecular gas mass determination with a standard method (Section 4.4). The former criterion allows us to confidently measure even weak $[CI](^3P_1 - ^3P_0)$ fluxes or put stringent upper limits at the expected line location. In fact, a non detection could be due to either intrinsic weak $[CI](^3P_1 - ^3P_0)$ emission or to the absence of frequency coverage owing to inaccurate redshifts. Significant offsets between optical/nearinfrared and sub-millimeter redshift estimates are not unusual, especially considering the heterogeneous original data catalogs in the literature and the different approaches to assess the redshift quality. Some of the

sources we selected did have initial low-quality flags in the COSMOS compilation. The requirement of alternative gas tracers excludes 2/29 extra-sources with a single $[CI](^3P_1 - {}^3P_0)$ line detection and no dust continuum or any CO emission covered. The rest of the sample not analyzed here is characterized by: (1) good coverage of the far-infrared SED, but low quality optical/near-infrared spectra and no sub-millimeter lines detection (7/29 sources) or ascertained wrong redshifts from CO lines that became available after our ALMA observations (7/29 objects). In the latter case, the $[CI](^3P_1 - ^3P_0)$ transition fell outside the covered frequency range or could not be identified unambiguously; (2) no detections in 3 or more followed-up submillimeter lines (4/29 galaxies), despite good quality flags associated with $z_{\rm opt/NIR}$ and good coverage of the far-infrared SED: this might be due to a wrong association with an optical/near-infrared counterparts or redshift quality assessment; (3) good quality $z_{\text{opt/NIR}}$, but serious blending and source misidentification in the far-infrared and sub-millimeter bands, which we could verify only a posteriori with new catalogs becoming available (3/29 sources); (4) a combination of low quality $z_{\rm opt/NIR}$ and bad coverage or even non-detection in the far-infrared SED based on the new catalogs superseding the previous compilations (6/29 galaxies). For these galaxies, the absence or a spectroscopic confirmation from a sub-millimeter line and/or an alternative gas tracer securely detected, either dust or CO(2-1), does not allow a proper assessment of $[CI](^3P_1 - {}^3P_0)$ as a proxy for the molecular gas content in our sample.

4

Respectively 100% and 95% of the 21 sources presented here are detected with a cumulative infrared signal-to-noise ratio SNR > 3 and > 5 in the "superdeblended" catalog by Jin et al. (2018, see below). The latter became available after our ALMA observations and superseded the PEP catalog in our analysis. Moreover, 16/21 galaxies lie on the main sequence at their redshift, 3/21 are classified as starbursts ($> 3.5 \times$ above the main sequence), and 2/21 suffer from a significant contribution from AGN emission (Figure 1). The main-sequence galaxies are on average $\sim 1.8 \times$ above the parametrization by Sargent et al. 2014, as expected from our selection.

A discussion of the whole sample and the detailed combined modeling of all the CO and [C I] transitions is postponed to a dedicated forthcoming paper (Valentino et al. in prep.).

2.2. Ancillary data

Our sample benefits from the excellent photometric and spectroscopic coverage available in COSMOS. In particular, we adopted the stellar masses listed in Laigle et al. (2016), consistent with the values derived by Muzzin et al. (2013), both modeling the UV to nearinfrared SEDs with standard recipes. Moreover, we modeled the "super-deblended" infrared photometry Jin et al. (2018) as in Magdis et al. (2012b) to derive the galaxy integrated far-infrared properties. The "superdeblending" of the highly confused far-infrared bands is based on an active choice of the radio and 24 μ m priors based on the galaxies spectral properties, reducing the blending degeneracies and resulting in well behaved flux density uncertainties (see Liu et al. 2018 for a detailed description of the method). Whenever available, we fit the emission from Spitzer/MIPS 24 μm (Sanders et al. 2007), Herschel/PACS (Lutz et al. 2011) and SPIRE bands (Oliver et al. 2012), JCMT/SCUBA2 (Geach et al. 2017), ASTE/AzTEC (Aretxaga et al. 2011), IRAM/MAMBO (Bertoldi et al. 2007), and ALMA continuum emission at $\sim 1.1 - 1.3$ mm (Section 2.3) with an expansion of the Draine & Li (2007, DL07) model library (Figure A.1 in Appendix). We further included a dusty torus component surrounding active galactic nuclei (AGN) following Mullaney et al. (2011) and subtracted this contribution from the total $L_{\rm IR}$ we derived. Therefore, $L_{\rm IR}$ always refers only to the component due to star formation for this sample. We then converted $L_{\rm IR}$ into SFR as SFR = $L_{\rm IR} [L_{\odot}]/(9.86 \times 10^9) M_{\odot} {\rm yr}^{-1}$ (Kennicutt 1998a, converted to a Chabrier IMF). The emission from the dusty torus is relevant ($\sim 40\%$ and > 95 % of $L_{\rm IR}$) in 2 sources, flagged everywhere as "AGN" hereafter. Moreover, their stellar masses are likely overestimated, due to significant AGN emission in the near-infrared bands. Therefore, for the purpose of this work, we will not include the AGN in any further step of the analysis. While fitting the SEDs, we included the upper limits in every band, modeling the nominal values weighted by their large uncertainties. We then bootstrapped the values within the observed errors to estimate the statistical uncertainties on the derived quantities. In Table 1 and 2, we report the $8-1000 \mu m$ total $L_{\rm IR}$ for all our galaxies, the contribution from dusty tori, and the total dust mass M_{dust} . We note that L_{IR} is well constrained for the vast majority of our sample, while $M_{\rm dust}$ critically relies on the availability of a measurement in the Rayleigh-Jeans tail of the dust emission.

2.3. ALMA [CI](1-0) and CO observations

We collected Atacama Large Millimeter Array (ALMA) Band 6 observations during Cycle 4 (Project ID: 2016.1.01040.S, PI: F. Valentino). Galaxies were

grouped in three scheduling blocks targeting $[CI](^3P_1 ^{3}P_{0}$) ($\nu_{\rm rest} = 492.161 \text{ GHz}$) and CO(4 - 3) ($\nu_{\rm rest} =$ 461.041 GHz) at $z \sim 1.15$, and $[CI](^3P_1 - {}^3P_0)$ only at $z \sim 1.28$ within contiguous spectral windows (SPWs) of 1.875 GHz and a requested spectral resolution of 7.8 MHz ($\sim 10 \text{ km s}^{-1}$). Two out of three of the blocks were fully observed, while the third was incomplete, resulting in a higher rms. Data were collected in configuration C40-1, corresponding to a synthesized beam of 2.0×1.7 ". Galaxies are generally not (or marginally) resolved, ensuring minimal flux losses. We reduced the raw data with the standard ALMA pipeline with CASA (McMullin et al. 2007). We then converted the calibrated data cubes to uvfits and analyzed them with GILDAS (Guilloteau & Lucas 2000). We extracted 1D spectra using PSFs and circular Gaussians models and fitting visibilities in the uv space with the iterative process described in Daddi et al. (2015). The $[CI](^3P_1 - ^3P_0)$ spectra are shown in Figure A.1 in Appendix. We looked for emission lines scanning the signal-to-noise ratio (SNR) spectrum. We measured fluxes as the weighted average flux density within the channels maximizing the SNR, times the velocity width covered by these channels. We further fit single or double Gaussians to the line profile to estimate total fluxes, generally $\sim 10\%$ larger than the fluxes measured over the number of channels maximizing the SNR. We finally adopted the first approach, applying a correction of 10% to the line fluxes. When multiple lines were available, we measured fluxes and upper limits on the same velocity width of the brightest line. These results agree with measurements leaving each line center and width free to vary. We measured integrated $[CI](^3P_1 - {}^3P_0)$ fluxes at $> 3\sigma$ in 18/21 sources down to an average rms/beam of $\sim 0.15~\mathrm{Jy~km~s^{-1}}$ for a line width of 400 km s⁻¹ and a final velocity resolution of $\sim 20-40 \text{ km s}^{-1}$. Fifteen out of 21 sources have [CI] detections significant at $> 4\sigma$. All the remaining sources have either one or multiple CO lines detected at $> 4\sigma$ at the same redshift (see next paragraph), allowing us to explore the SNR < 4 regime or to put secure upper limits on [C I]. We simultaneously measured the continuum emission at observed ~ 1.3 mm over 7.5 GHz assuming an intrinsic slope of $\nu^{3.5}$ ($\beta = 1.5$). We detected significant continuum emission at 3σ in 14/21 sources down to an rms of ~ 0.07 mJy on the full frequency range.

From the same observing campaign, we similarly measured CO (4-3) fluxes at $> 4\sigma$ significance in all 14 galaxies with frequency coverage of this line. Moreover, 15 and 11 galaxies of our sample have been observed by ALMA Bands 6 and 3 independent observations tar-

geting CO(5-4) and CO(2-1), respectively (Project IDs: 2015.1.00260.S, 2016.1.00171.S, PI: Daddi; Daddi et al. in prep.). Data were collected at similar spatial resolutions, reduced and analyzed as we described above. For the purpose of the present work, we used high-SN CO emissions to (1) fix the center of the circular Gaussian or PSF to extract the spectrum, the central line frequency, and the width of $[CI](^3P_1 - ^3P_0)$; (2) to measure gas masses from CO(2-1); and (3) to measure mm continuum emission. We do not find evidence of systematically broader or narrower [CI] lines than CO transitions, when the velocity width is let free to vary. We significantly detected CO (2-1) and CO (5-4) in all 11 and 15 targeted galaxies, and continuum emission at observed $\sim 3 - 1.1$ mm for 1/11 and 8/15 galaxies covered by Band 3 and 6 observations, respectively. This brings the overall number of sources with ~ 1 " spatial resolution mm continuum detection to 17/21.

We report the observed $[CI](^3P_1 - ^3P_0)$ and CO(2-1) fluxes and L' luminosities in Table 1. A full compilation including the CO(4-3) and CO(5-4) fluxes will be discussed in future work (Valentino et al. in prep.).

3. LITERATURE DATA

We compared our results with observations available in literature. We collected and homogenized line luminosities and galaxy properties to properly match our conventions.

3.1. Local galaxies

This sample is drawn from the public compilation of all Herschel/Fourier Transform Spectrometer (FTS) observations in the Herschel Science Archive of local galaxies by Liu et al. (2015, L15 hereafter). sources are part of the IRAS Revised Bright Galaxy Sample (Sanders et al. 2003) and covered at $70-160~\mu\mathrm{m}$ by Herschel/PACS. FTS simultaneously spanned the 446 - 1543 GHz frequency interval, covering all CO lines with $J_{\rm up}=4-13$, the $[{\rm C\,I}](^3P_1-^3P_0)$ and $[CI](^3P_2 - ^3P_1)$ lines, and several other transitions. L15 reduced the FTS raw data with the SPIRE v.12 calibration products and the *Herschel* Interactive Processing Environment pipelines (HIPE v12.1.0, Ott 2010). They extracted all the lines simultaneously with customized optimized HIPE spectral line fitting scripts on the unapodized spectra with varied-width Sincconvolved Gaussian (SCG) functions, and they estimated the line flux errors from the rms of the spectra near each line (see L15 for further details). In total we retrieved 32 galaxies (out of 146 in the compilation by L15) with a $[CI](^3P_1 - ^3P_0) > 3\sigma$ detection up

to $z\sim 0.03$. We corrected the far-infrared luminosities integrated over the $40-400~\mu\mathrm{m}$ interval reported in L15 to match the $8-1000~\mu\mathrm{m}$ total L_{IR} we adopt here, by multiplying by a factor $1.2\times$. We obtained this value by comparing the original $L_{\mathrm{FIR}}(40-400~\mu\mathrm{m})$ with $L_{\mathrm{IR}}(8-1000~\mu\mathrm{m})$ from SED modeling as described in Section 2.2 for the subset of galaxies from the Great Observatories All-Sky LIRGs Survey (GOALS, Armus et al. 2009) included in L15. Emission line fluxes and infrared luminosities have been beammatched as described in L15 and reported to the total, galaxy-integrated values back-applying the beam correction based on PACS photometry ($I_{[\text{CI}]}$ (L15, total) = $I_{[\text{CI}]}$ (L15, beam) \times $F_{\mathrm{PACS,total}}/F_{\mathrm{PACS,beam}}$.

6

We further cross-matched the sample in L15 with the alternative compilation of Herschel/FTS observations and low-J CO transitions from ground based facilities by Kamenetzky et al. (2016, K16). First, we checked that the FTS beam measurements for galaxies with $[CI](^3P_1 - {}^3P_0)$ detections in both samples were consistent. Then, we corrected the CO line measurements within the fixed 43.5" beam in K16 (their Table 3) to the galaxyintegrated values. We multiplied the fluxes in K16 by $\eta_{\text{beam}} = I_{[C_I]}(\text{L15, total})/I_{[C_I]}(\text{K16, 43.5"beam}), \text{ where}$ $I_{\rm [CI]}({\rm L}15,{\rm total})$ are the galaxy-integrated $[{\rm CI}](^3P_1$ - $^{3}P_{0}$) fluxes in L15 and $I_{[C_{I}]}(K16, 43.5"beam)$ the $[CI](^3P_1 - {}^3P_0)$ fluxes within a fixed 43.5" beam by K16. The median correction factor is $2\times$ and $1.25\times$ for sources closer and farther than 20 Mpc, respectively. When multiple estimates of the same low-J CO transitions were available, we assumed a SNR-weighted average as representative of the line flux. Note that the line ratios do not suffer from extra uncertainty due to the beam correction than what reported in the K16 compilation. Moreover, for the closest sources the final values might be representative mainly of the nuclear regions. Out of 32 sources with a $[CI](^3P_1 - {}^3P_0)$ detection, 29 and 26 have a CO(1-0) and CO(2-1) $> 3\sigma$ detection, respectively.

We further estimated the stellar masses of 20/32 galaxies of the FTS sample with available $K_{\rm s}$ -band imaging from 2MASS (Skrutskie et al. 2006) averaging the values obtained following Arnouts et al. (2007, Eq. 2) and Juneau et al. (2011, Eq. B1, B2). We checked these results against the full UV to near-infrared SED fitting for a subset of 32 objects in common between the whole compilation of L15 and the sample studied by U et al. (2012), finding consistent results. Figure 1 shows the location of the galaxies with a $> 3\sigma$ [C1]($^3P_1 - ^3P_0$)

detection in the M_{\star} – SFR($L_{\rm IR}$) plane, typically lying above the main sequence at their redshift. Since AGN can contaminate both $L_{\rm IR}$ and the $K_{\rm s}$ -band derived M_{\star} , we flagged 12/32 known active galaxies listed in the catalog by Véron-Cetty & Véron (2010, VCV10). Among the non-active galaxies, 70% (14/20) are LIRGs ($L_{\rm IR} > 10^{11}~L_{\odot}$). For the local sample, we do not attempt to disentangle the contribution of the dusty torus to the total $L_{\rm IR}$. In the rest of the paper, we will refer to the sample of local galaxies as "FTS Local" or "Local LIRGs", when they do not host a bright AGN.

3.2. High-redshift sub-mm galaxies and quasars

We assembled a sample of sub-millimeter galaxies (SMGs) and quasars (QSOs) with $[CI](^3P_1 - ^3P_0)$ coverage from Walter et al. (2011, W11), Alaghband-Zadeh et al. (2013, AZ13), and Bothwell et al. (2017, B17). We refer the reader to these papers for fully detailed references, sample selection, and observations. W11 and AZ13 targeted or collected information on typical SMGs at $z \sim 2.5 - 4$ detected at $\sim 850 \ \mu \text{m}$, with a tail of well-studied QSOs extending up to $z \sim 6.5$. A large fraction of these sources are gravitationally magnified up to $\sim 30 \times$ and are detected in CO (3 – 2) and CO(4-3). Similarly magnified are 1.4 mm detected sub-millimeter galaxies in B17, identified in a blank-field survey with the South Pole Telescope (SPT, Vieira et al. 2010; Weiß et al. 2013), with spectroscopic information on high- (Weiß et al. 2013, B17) and low-J transitions (CO(2-1), Aravena et al. 2016). The final sample consist of 33 galaxies, 25/33 with $[CI](^3P_1 - ^3P_0)$ detections at $> 3\sigma$. We re-derived their total $L_{\rm IR}$ and dust masses $M_{\rm dust}$, modelling their far-infrared SED applying the same method described in Section 2.2. The SPT-SMGs galaxies are all detected in SPIRE 250, 350, and 500 μ m. LABOCA 870 μm , SPT 1.4 and 2.0 mm, and ALMA 3 mm bands (Weiß et al. 2013). The SEDs of SMGs and QSOs from W11 and AZ13 are sampled less homogeneously, but ensuring a good coverage of both the peak and the Rayleigh-Jeans of the dust emission in the vast majority of cases. Applying our recipes, we estimate total $L_{\rm IR}(8-1000\,\mu m)\sim 1.5\times (\sim 3\times)$ larger than the original values derived with modified black body curves for SMGs (QSOs), including a correction for the different integration limits. We also estimate $M_{\rm dust}$ for the SPT-SMGs systematically larger than previously reported (Aravena et al. 2016). The systematic differences in $L_{\rm IR}$ and $M_{\rm dust}$ fully depend on the adopted models (modified black body law, DL07) and their parameters (effective dust emissivity index β , dust mass absorption coefficient κ , peak temperature, Magdis et al. 2012b). The discrepancy in $L_{\rm IR}$ is larger for QSO hosts owing to

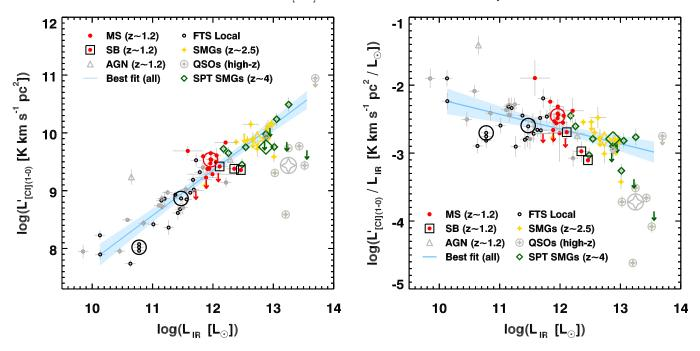


Figure 2. Total $L_{\rm IR}$ - $L'_{[C\,1]^3P_1-^3P_0}$ relation. In both panels, red filled circles represent our > 3σ detected MS galaxies at $z\sim 1.2$; open black squares: SBs; gray triangles: AGN; open black circles: local FTS > 3σ detections without AGN signatures; open gray circles: local FTS > 3σ detections listed as active in VCV10; yellow stars: SMGs at $z\sim 2.5$ from W11 and AZ13; gray stars and open circles: high-redshift QSOs from W11; green open diamonds: SPT SMGs at $z\sim 4$ from B17. Arrows mark 3σ upper limits on $L'_{[C\,1]^3P_1-^3P_0}$. The solid light blue line and hatched area represent the best linear regression model of all SF-dominated galaxies (i.e., excluding QSOs and AGN) and the 95% confidence interval. The $L_{\rm IR}$ of QSOs is dominated by the emission of the dusty torus, which is included in the estimate, at odds with the rest of SF-dominated galaxies. The larger symbols mark the median values for each sample. We split the FTS local sample in two bins with a threshold at $L_{\rm IR}=10^{11}~L_{\odot}$, the formal limit for the LIRG classification. Left: $L_{\rm IR}-L'_{[C\,1]^3P_1-^3P_0}$ relation, a proxy for the SFR and gas mass relation. Right: $L_{\rm IR}-L'_{[C\,1]^3P_1-^3P_0}/L_{\rm IR}$ is a proxy for the gas depletion timescale $\tau_{\rm dep}\propto 1/{\rm SFE}$, dropping with increasing $L_{\rm IR}$ and shorter for starbursting galaxies than for sources on the MS.

the dusty torus emission mid-IR bands, where the difference between modified black body curves and DL07 models is more significant. All the quantities presented here have been corrected for magnification. Moreover, we correct the $L_{\rm IR}$ luminosities of SMGs for the contribution of AGN similarly to what we did for the MS sample. We find only 1 (SPT-)SMG whose SED is dominated by a dusty torus ($\sim 70\%$ of the total $L_{\rm IR}$). For known bright QSOs at high-redshift in W11, we do not attempt to separate the star formation and AGN contributions to $L_{\rm IR}$, being largely dominated by the latter. However, we will not consider these sources in the analysis any further, but simply show their position in the various plots for reference. Stellar masses are not available for this high-redshift sample, apart from 2 sources listed in B17. Therefore, we could not place these objects in the M_{\star} – SFR plane and canonically define them as SB or MS based on these observables. However, their observed ISM conditions, gas and SFR densities, and SFEs generally distinguish SMGs from MS galaxies (e.g., Daddi et al. 2010a; Genzel et al. 2010; Bothwell

et al. 2013; Casey et al. 2014). In the following, we will label "SMGs ($z \sim 2.5$)" the sample from W11 and AZ13, "QSOs (high-z)" the sources with clear AGN signatures from W11, and "SPT SMGs ($z \sim 4$)" the sample by B17. Moreover, we will consider SMGs as starbursting systems and not typical MS galaxies.

4. ANALYSIS AND RESULTS

4.1. The
$$L_{IR} - L'_{[CI]^3P_1 - {}^3P_0}$$
 relation

Following Solomon & Vanden Bout (2005), we computed the $[CI](^3P_1 - ^3P_0)$ line luminosities in K km s⁻¹ pc², representing the integrated source brightness temperature:

$$L'_{\rm line} \, [{\rm K\,km\,s^{-1}\,pc^2}] = 3.25 \times 10^7 \, S_{\rm line} \, \Delta v \, \nu_{\rm obs}^{-2} (1+z)^{-3} D_{\rm L}^2 \end{tabular}$$

where $S_{\text{line}} \Delta v$ is the measured velocity-integrated line flux in Jy km s⁻¹, ν_{obs} the observed line frequency in GHz, z the redshift of the source, and D_{L} is the luminosity distance in Mpc. Figure 2 shows the relation between the total L_{IR} and $L'_{[\text{C I}]^3P_1-{}^3P_0}$ for our sample of MS galaxies and the literature compilation of star-

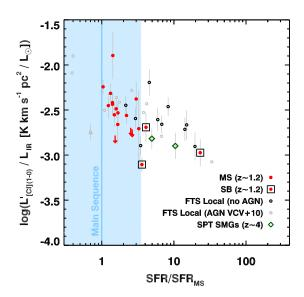


Figure 3. Distance from the main sequence - $L'_{[\text{CI}]^3P_1-{}^3P_0}/L_{\text{IR}}$ plane. Red filled circles mark our sample of MS galaxies at $z\sim 1.2$ with a $>3\sigma$ [CI](${}^3P_1-{}^3P_0$) detection. Black squares indicate SBs. Open black and gray circles represent the local comparison sample of non-active and active galaxies covered by FTS observations (Liu et al. 2015). Green open diamonds indicate the 2 SPT-SMGs at $z\sim 4$ with an estimate of M_{\star} from B17. Arrows mark 3σ upper limits on $L'_{[\text{CI}]^3P_1-{}^3P_0}$. The MS is parametrized as in Sargent et al. (2014).

bursting sources at various redshifts. Both a Spearman's rank and a Pearson's correlation coefficients show that the two quantities are correlated, considering all $> 3\sigma$ detected sources and excluding QSOs and AGN ($\rho_{\text{Spearman}} = 0.8990, \rho_{\text{Pearson}} = 0.9024$). We further applied a linear regression analysis on $\log(L_{\rm IR}) - \log(L'_{\rm [C_I]^3P_1-^3P_0})$ both using a Bayesian (LINMIX_ERR.PRO, Kelly 2007) and a χ^2 -minimization algorithm (MPFIT.PRO, Markwardt 2009) taking into account the uncertainties on both $L_{\rm IR}$ and $L'_{[{\rm C}\,{\rm i}]^3P_1\,-\,^3P_0},$ and including the upper limits on $L'_{[CI]^3P_1-{}^3P_0}$ in the Bayesian fit. Since $L_{\rm IR}$ and $L'_{\rm [C\,I]^3P_1\,-\,^3P_0}$ are proxies for the integrated SFR and $\dot{M}_{\rm gas},$ this relation is analogous to the Schimdt-Kennicutt relation (Schmidt 1959; Kennicutt 1998b, with the X and Y axes generally inverted). The two algorithms we applied provided fully consistent results within the uncertainties, and the effect of upper limits is negligible. We modeled a total of 57 [CI](${}^{3}P_{1} - {}^{3}P_{0}$)-detected galaxies and 10 upper limits. The Bayesian best fit model returns a sublinear slope of 0.78 ± 0.05 with an observed scat-

ter of $\sigma = 0.26$ dex. Note that AGN and QSOs are not included in the fit, nor in the calculation of σ . Their location in the diagram is mainly driven by their $L_{\rm IR}$, boosted by the contribution of the dusty tori in the mid-IR regime, adding to moderately larger intrinsic luminosities than high-redshift SMGs at fixed $L'_{[C_1]^3P_1-{}^3P_0}$ (W11). Modeling only the starbursting population (i.e., SB at $z \sim 1.2$, local LIRGs, and SMGs) provides a similar slope of 0.79 ± 0.06 . Interestingly, these values are consistent with that of the $\log(L_{\rm IR}) - \log(L'_{\rm CO(1-0)})$ relation (0.81 ± 0.03, Sargent et al. 2014), reinforcing the connection between [CI] and CO. Moreover, our MS detected galaxies appear to have larger $L'_{[{\rm C}\,{\rm I}]^3P_1\,-\,^3P_0}/L_{\rm IR}$ ratios than SMGs. This is more evident in the right panel of Figure 2. The mean value of $\log(L'_{[C_1]^3P_1-{}^3P_0}/L_{IR} [K \,\mathrm{km} \,\mathrm{s}^{-1} \,\mathrm{pc}^2 \,\mathrm{L}_{\odot}^{-1}])$ for 16 MS galaxies is (-2.43 ± 0.06) , $\sim 2 \times$ higher than the mean for SMGs at $z \sim 2.5 ((-2.77 \pm 0.07) \text{ dex})$ and SPT-SMGs at $z \sim 4 ((-2.80 \pm 0.07) \text{ dex})$, where the uncertainties represent the error on the mean. We included the upper limits on $[CI](^3P_1 - {}^3P_0)$ in the calculation using a survival analysis (KM estimator, Kaplan & Meier 1958). This difference is significant at a $\sim 4\sigma$ level. The median values are fully consistent with the mean. The ratio for the local sample of non-active galaxies is consistent with the estimate for MS galaxies, but it suffers from a very large dispersion. In Figure 3 we further show the $L'_{[{\rm C}\,{\rm I}]^3P_1\,-\,^3P_0}/L_{\rm IR}$ ratio as a function of the distance from the main sequence ($\Delta SFR = SFR/SFR_{MS}$) as parametrized in Sargent et al. (2014). We included only sources with a stellar mass estimate, i.e., all our galaxies, part of the local LIRGs, and 2 SPT-SMGs. Excluding galaxies with AGN signatures, the $L'_{[CI]^3P_1-{}^3P_0}/L_{IR}$ ratio and Δ SFR are mildly anti-correlated ($\rho_{\text{Spearman}} = -0.6940$, $\rho_{\rm Pearson} = -0.5961$), with SMGs and SBs at $z \sim 1.2$ showing systematically lower ratios than MS galaxies, as in Figure 2. However, the scarce statistics of lower main-sequence sources and SBs with available M_{\star} prevents us from deriving more definitive conclusions. From a physical perspective, since $L'_{[C_1]^3P_1-{}^3P_0}$ traces the gas mass and $L_{\rm IR}$ the SFR, their ratio is a proxy for the gas depletion timescale $\tau_{\rm dep}$. The observed trends would then suggests a drop of this quantity (or equivalently an increment of SFE) with increasing $L_{\rm IR}$ and distance from the main sequence, analogously to the well established correlations observed for CO (e.g., Daddi et al. 2010b; Magdis et al. 2012b; Genzel et al. 2015; Tacconi et al. 2018).

4.2. The
$$L'_{[Ci]^3P_1-{}^3P_0} - L'_{CO(2-1)}$$
 relation

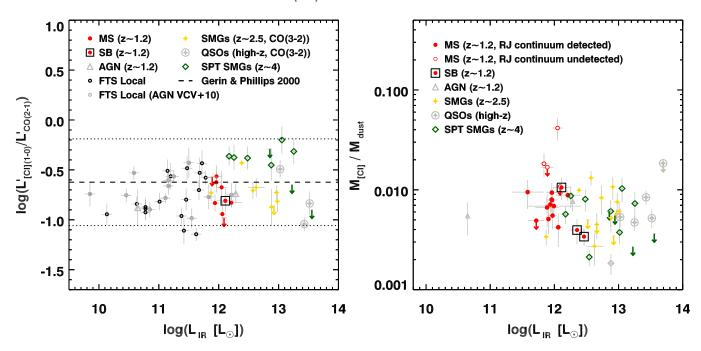


Figure 4. Left: $L'_{[\text{CI}]^3P_1-^3P_0}-L'_{\text{CO}(2-1)}$ as a function of total L_{IR} . Symbols are coded as in Figure 2 and reported in the legend. The dashed and dotted black lines mark the average ratio and its scatter observed in a sample of local spirals, mergers, and low-metallicity galaxies from Gerin & Phillips (2000). Arrows mark 3σ upper limits on $L'_{[\text{CI}]^3P_1-^3P_0}$. Right: $M_{[\text{CI}]}/M_{\text{dust}}$ as a function of L_{IR} . Symbols are coded as in Figure 2 and reported in the legend. Open red circles mark sources without a reliable continuum detection in the Rayleigh-Jeans tail, thus having an uncertain dust mass. In both panels, the L_{IR} of QSOs includes the emission of the dusty tori, at odds with the rest of SF-dominated galaxies.

Figure 4 shows the $L'_{[\text{C I}]^3P_1-{}^3P_0}/L'_{\text{CO}(2-1)}$ ratio as a function of the total L_{IR} . The observed ratio is similar in MS and SB galaxies at $z \sim 1.2$, local LIRGs, and high-redshift SMGs, within a fairly large scatter. We estimate a mean value of $\log(L'_{[C_1]^3P_1-{}^3P_0}/L'_{CO(2-1)}) =$ (-0.69 ± 0.04) with an observed scatter of 0.23 dex for $37 > 3\sigma$ -detected galaxies, largely dominated by the intrinsic dispersion of 0.20 dex. The inclusion of 6 upper limits with a survival analysis provides consistent values (the mean from the Kaplan & Meier (1958) estimator is $\log(L'_{[\text{C}_{\text{I}}]^3P_1 - {}^3P_0}/L'_{\text{CO}(2-1)}) = (-0.72 \pm$ 0.04), with a standard deviation of 0.24 dex). The $L'_{[\text{C I}]^3P_1 - {}^3P_0}/L'_{\text{CO}(2-1)}$ ratio does not appear to vary with $L_{\rm IR}$. For the W11 sample we converted CO (3-2)to CO (2-1) applying a $r_{32} = L'_{CO(3-2)}/L'_{CO(2-1)} =$ 0.62 (Bothwell et al. 2013). Adopting ratios close to the original W11 paper $(r_{32} = 1 \text{ for fully thermal-}$ ized gas) would result in ratios $\sim 60\%$ larger, bringing them closer to the values from B17. For the FTS sample we used the observed CO (2-1) luminosities when available (26/32 galaxies), and converted CO(1-0)to CO (2-1) fixing $r_{21}=L'_{\rm CO(2-1)}/L'_{\rm CO(1-0)}=0.84$ for 3 more sources. These ratios are consistent with the observations in local spirals, mergers, and lowmetallicity galaxies and their large scatter reported in

Gerin & Phillips (2000), once corrected for the small excitation bias between CO (2 - 1) and CO (1 - 0) ($\log(L'_{[C\,I]^3P_1-{}^3P_0}/L'_{CO(2-1)}) = -0.7 \pm 0.4$ dex, with extreme values of $\log(L'_{[C\,I]^3P_1-{}^3P_0}/L'_{CO(2-1)}) \sim -1.4$ and 0). Therefore, $[C\,I]({}^3P_1-{}^3P_0)$ and low-J CO transitions appear to be correlated on >kpc-scales regardless of galaxy type, total $L_{\rm IR}$, and redshift, although with substantial scatter due to object by object variations, given the small measurement errors on fluxes.

4.3. Neutral atomic carbon masses

Following Weiß et al. (2005), the mass of atomic carbon is derived straightforwardly from $L'_{[C1]^3P_1-{}^3P_0}$ as:

$$M_{[CI]} = 5.706 \times 10^{-4} Q(T_{ex}) \frac{1}{3} e^{23.6/T_{ex}} L'_{[CI]^3 P_1 - {}^3 P_0} [M_{\odot}]$$
(2)

where $Q(T_{\rm ex})=1+3{\rm e}^{-23.6{\rm K/T_{\rm ex}}}+5{\rm e}^{-62.5{\rm K/T_{\rm ex}}}$ is the partition function of [CI] and $T_{\rm ex}$ the excitation temperature. We cannot derive $T_{\rm ex}$ from the $L'_{[{\rm CI}]^3P_2-{}^3P_1}/L'_{[{\rm CI}]^3P_1-{}^3P_0}$ ratio, since [CI](${}^3P_2-{}^3P_1$) is unavailable for our sample of MS galaxies at $z\sim 1.2$. Therefore, we assume a fixed [CI] excitation temperature $T_{\rm ex}=30$ K for all galaxies. W11 reports a $\langle T_{\rm ex}\rangle=29.1\pm6.3$ K for their overall sample of SMGs and QSOs and we derive $\langle T_{\rm ex}\rangle=25\pm1$ K for part of

the FTS local sample with both $[C\,I](^3P_1 - ^3P_0)$ and $[C\,I](^3P_2 - ^3P_1)$. A typical value of 30 K has also been previously adopted by AZ13 and B17. Assuming the dust temperature that we estimate from the far-infrared SED modeling as a first guess for the $[C\,I]$ $T_{\rm ex}$, we find similar results $(\langle T_{\rm dust} \rangle = 31 \pm 1$ K for the MS calibration sample, and $\langle T_{\rm dust} \rangle = 36 \pm 2$ K for the SBs). Note that the total neutral carbon mass is insensitive to $T_{\rm ex}$ above 20 K (Weiß et al. 2005), so the exact choice of this parameter is not critical above this threshold, which is unlikely in the samples studied here. We report the total $M_{[C\,I]}$ masses in Table 2.

4.4. Gas masses from dust and CO

We estimated the total gas masses (including a $1.36\times$ contribution from helium) for our sample of MS galaxies using both dust masses from SED modeling and CO(1-0) or CO(2-1) as gas tracers, when available. In both cases we adopted a metallicity-dependent conversion factor as described in Magdis et al. (2012b)¹. Note that this approach includes the atomic hydrogen HI in the gas mass estimate, a significant contributor to the total gas mass only at low redshift. We derived metallicities converting stellar masses and SFR with the Fundamental Metallicity Relation (Mannucci et al. 2010). The derived metallicities are generally consistent with the solar value $(12 + \log(O/H)_{\odot} = 8.69$, Asplund et al. 2009). We estimate an average gas-to-dust conversion factor of $\langle \delta_{\rm GDR} \rangle \sim 87$ and $\langle \alpha_{\rm CO} \rangle \sim 3 \ M_{\odot}/{\rm K \ km \ s^{-1} \ pc^2}$. We assumed a $L'_{CO(2-1)}/L'_{CO(1-0)}$ ratio of $r_{21} = 0.84$ to convert CO(2-1) into total gas masses when necessary (Magdis et al. 2012b; Bothwell et al. 2013). We further derived total gas masses for our SBs at $z \sim 1.2$, LIRGs and high-redshift SMGs fixing the conversion factors to $\alpha_{\rm CO} = 0.8~M_{\odot}/({\rm K~km~s^{-1}~pc^2})$, and $\delta_{\rm GDR} = 30$. The final error budget includes the uncertainties on the observed CO fluxes and dust mass from SED modeling (Section 2.2). We further include a 0.2 dex statistical error on $\alpha_{\rm CO}$ and $\delta_{\rm GDR}$, mimicking the uncertainty on the metallicity-dependent parametrization in Magdis et al. (2012b). Possible larger systematic uncertainties affecting the gas masses are not listed in the error budget (e.g., Kamenetzky et al. 2017 for a study of the local LIRGs).

Figure 4 shows that the $M_{\rm [C\,I]}/M_{\rm dust}$ ratios of SMGs appear similar to the values for our MS and SB galax-

ies at $z \sim 1.2$, albeit with substantial scatter. We estimate a mean ratio of $\log(M_{\rm [C\,I]}/M_{\rm dust}) = (-2.20 \pm 0.03),$ with an observed scatter of $\sigma = 0.19$ dex dominated by an intrinsic dispersion of 0.15 dex for $33 > 3\sigma$ detected galaxies. The inclusion of 11 upper limits with a survival analysis provides a consistent result $(\log(M_{\rm [C\,I]}/M_{\rm dust}) = (-2.26 \pm 0.04), \ \sigma = 0.23 \ {\rm dex}).$ Note that we excluded active galaxies, QSOs, and galaxies without a detection of the dust continuum from this calculation. Moreover, the SMGs from B17 at $z \sim 4$ appear to have fainter CO (2-1) emission than the sample from W11 at $z \sim 2.5$ at fixed dust mass, assuming the SLED ratios from Bothwell et al. (2013) (Section 4.2). This is likely the result of a combination of different factors, including the gas excitation properties of individual SMGs; a redshift effect due to the evolution of the strength of the radiation field $\langle U(z) \rangle \propto L_{\rm IR}/M_{\rm dust}$; the different selection techniques; and the heterogeneity of the SMG population (Carilli & Walter 2013).

4.5. The abundance of neutral atomic carbon in galaxies

While not requiring a standard α or X factor as optically thick ¹²CO transitions, [CI] line luminosities can be converted into total gas masses only with prior knowledge of the abundance of carbon in the neutral atomic phase [C_I]/[H₂]. Such a conversion is necessary for any species other than H₂, the dominant form of molecular gas. We derived the atomic carbon abundances as $[C_I]/[H_2] = M_{[C_I]}/(6M_{H_2})$, using the M_{H_2} estimates from dust and CO. Notice that $M_{\rm H_2}$ does not include the helium contribution. Previous works adopted this or alternative approaches, providing atomic carbon abundance estimates in a variety of environments at different redshifts (e.g., Stutzki et al. 1997; Ikeda et al. 2002; Weiß et al. 2003, 2005; Israel et al. 2015, W11, AZ13 and B17 among the others). Here we redetermined the abundances based on a homogeneous set of assumptions, so to directly compare datasets in a consistent way. The discrepancies among our estimates and the ones in the original papers arise mainly from the choice of galaxies representative of the various populations (e.g., we exclude QSOs from the calculations), and different assumption (gas conversion factors, CO excitation ladder, inclusion or not of upper limits, dust- or CO-based gas masses, etc). First, we show the distribution of the estimated abundances for the MS sample at $z \sim 1.2$ in Figure 5. The mean values are $\log([C_1]/[H_2]) = (-4.7\pm0.1)$ and (-4.8 ± 0.2) adopting $M_{\rm H_2}({\rm dust})$ and $M_{\rm H_2}({\rm CO})$, respectively. The uncertainties represent the standard deviation of the observed distributions for 12 MS galaxies with detected continuum emission in the Rayleigh-

 $^{^1}$ Magdis et al. (2012b) reported an intercept of 12.8 in their parametrization of $\alpha_{\rm CO}(12+\log({\rm O/H}))$ (Eq. 8), not matching their Figure 5 (right). The correct value adopted here is 12.6. The parametrization of $\delta_{\rm GDR}(12+\log({\rm O/H}))$ is identical to Magdis et al.

Jeans tail and $[CI](^3P_1 - ^3P_0)$ coverage (11 detections and 1 upper limit) when using $M_{\rm H_2}$ (dust), and for 8 objects with $[CI](^3P_1 - ^3P_0)$ coverage (6 detections and 2 upper limits) and CO (2-1) detections in the case of $M_{\rm H_2}({\rm CO})$. We excluded 1 MS source with continuum detection due to unsuccessful far-infrared photometric deblending. We included the upper limits on $[CI](^3P_1 - ^3P_0)$ using a survival analysis, but their effect is negligible. The $[CI]/[H_2]$ in MS galaxies at $z \sim 1.2$ is consistent with the observed values in highly obscured clouds of the Milky Way $(\log([C_1]/[H_2]) \sim -5.7, -4.7$ depending on the dust attenuation, Frerking et al. 1989, Figure 5), and it is lower than the typically assumed abundance of $\log([C_1]/[H_2]) = -4.5$ (Weiß et al. 2003). For reference, we also show the distributions including SBs and the AGN-dominated objects. We remark that the abundances presented in this work are global, galaxy-integrated estimates, while local measurements often focus to individual clouds. A direct comparison should be drawn with caution, as it would be natural to find lower abundances on global scales, if [CI] and H₂ are not fully cospatial. We similarly rederived the atomic carbon abundances for the literature sample, using both $M_{\rm H_2}({\rm CO})$ and $M_{\rm H_2}({\rm dust})$ when available. For the local sample of 17 sources without AGN signatures and CO (1-0) detections we find $\log([C_1]/[H_2]) =$ (-4.2 ± 0.2) ; for the SPT-SMGs at $z \sim 4$ from B17, $\log([C_1]/[H_2]) = (-3.9 \pm 0.1)$ and (-4.3 ± 0.2) using CO(2-1) and dust, respectively; for SMGs at z > 2.5from W11 and AZ13, $\log([C_1]/[H_2]) = (-4.2 \pm 0.1)$ and (-4.3 ± 0.2) using CO (2-1) and dust, respectively. The uncertainties represent the dispersion of the distributions in Figure 5 and include upper limits with a survival analysis. Note that $[C_I]/[H_2] = M_{[C_I]}/(6 M_{H_2})$ faithfully represents the abundance of atomic carbon relative to the molecular hydrogen H₂, a good approximation for the total gas mass $M_{\rm gas}$ at high redshift. However, both $M_{\rm H_2}({\rm dust})$ and $M_{\rm H_2}({\rm CO})$ formally include HI, which might be the dominant phase in local systems. Removing HI and considering the molecular gas phase only would further increase the $[CI]/[H_2]$ values reported here above for the local galaxies.

5. THE CALIBRATION OF [C I] AS A GAS TRACER IN GALAXIES

5.1. The limitations of a fully empirical approach

So far we have proven that it is feasible to detect $[C\,I](^3P_1\ -\ ^3P_0)$ lines not only in distant, extreme, and often lensed systems, such as SMGs and QSOs, but also in normal MS galaxies at moderately high redshifts. We showed the existence of a $L_{\rm IR}$ – $L'_{\rm [C\,I]^3P_1\ -\ ^3P_0}$ correlation similar to the standard $L_{\rm IR}$ – $L'_{\rm CO(1-0)}$ relation, with

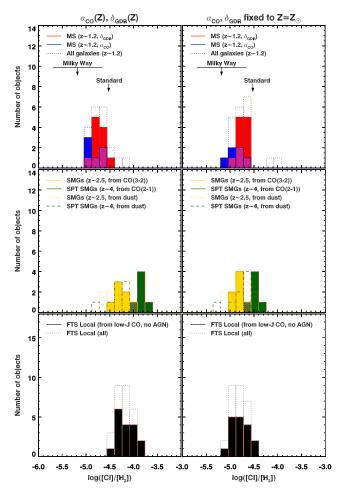


Figure 5. Atomic carbon abundances. Top: The red and blue filled histograms show the distribution of the carbon abundances [CI]/[H2] for our sample of MS galaxies with $> 3\sigma$ detections of $[CI](^3P_1 - {}^3P_0)$ derived using a dustand CO (2-1)-based $M_{\rm H_2}$ (Section 4.4). The black segment and arrows show the range of values reported in literature for regions of the Milky Way $(\log([C_{I}]/[H_{2}]) = (-5.7, -4.7),$ Frerking et al. 1989), and the commonly adopted value of $\log([C_1]/[H_2]) = -4.5$ (Weiß et al. 2003). The dotted lines mark the distributions including SBs and AGN, when possible. Center: The yellow and green filled (dashed/dotted) histograms show [CI]/[H2] for SMGs from W11/AZ13 and B17 using a CO (2-1)- (dust)-based $M_{\rm H_2}$. Bottom: The black filled histograms show [CI]/[H2] for local LIRGs without AGN signatures using CO-based $M_{\rm H_2}$. The dotted histogram show the abundance distribution for the whole FTS sample, including active galaxies. Left panels: $M_{\rm H_2}$ derived adopting metallicity dependent $\alpha_{\rm CO}$ and $\delta_{\rm GDR}$ for MS galaxies and fixed $\alpha_{\rm CO}=0.8~M_{\odot}/({\rm K~km~s^{-1}~pc^2})$ and $\delta_{\rm GDR}=30$ for SBs, local FTS galaxies, and SMGs. Right panels: Universal $\alpha_{\rm CO}=3.3~M_{\odot}/({\rm K~km~s^{-1}~pc^2})$ and $\delta_{\rm GDR}=85$, following Magdis et al. (2012b) and fixing $Z = Z_{\odot}$ for all galaxies.

 $L'_{[\text{C}\,\text{I}]^3P_1\,-\,^3P_0}/L_{\text{IR}}$ ratios systematically decreasing with increasing L_{IR} and distance from the main sequence. The strong correlation between $L'_{[\text{C}\,\text{I}]^3P_1\,-\,^3P_0}$ and L_{IR} makes the latter a useful tool to predict $[\text{C}\,\text{I}]$ emission in distant galaxies. Moreover, the roughly constant $L'_{[\text{C}\,\text{I}]^3P_1\,-\,^3P_0}/L'_{\text{CO}(2-1)}$ and $M_{[\text{C}\,\text{I}]}/M_{\text{dust}}$ ratios on kpc-scales, regardless of total L_{IR} , galaxy type, and redshift, reinforce the connection between $[\text{C}\,\text{I}]$, CO, and dust, supporting the use of $[\text{C}\,\text{I}]$ as a molecular gas tracer.

Constant $L'_{[\text{C I}]^3P_1-{}^3P_0}/L'_{\text{CO}(2-1)}$ and $M_{[\text{C I}]}/M_{\text{dust}}$ ratios directly translate into systematically lower neutral atomic carbon abundances in MS galaxies than in SBs/SMGs, owing to the canonical empirical $\alpha_{\rm CO}$ and gas-to-dust $\delta_{\rm GDR}$ conversion factors ($\alpha_{\rm CO} \sim 4$ – $0.8~M_{\odot}/({\rm K~km~s^{-1}~pc^2})$ and $\delta_{\rm GDR} \sim 85-30$ for MS and SB galaxies, respectively). Assuming identical conversion factors, the abundances are similar in MS galaxies and SBs/SMGs (we show the case of constant $\alpha_{\rm CO}, \delta_{\rm GDR}(Z=Z_{\odot})$ in Figure 5). In other words, the well-known uncertainties of the standard CO and dust tracers affect the *empirical* calibration of [CI]. This practically limits the use of this potentially superior tracer of gas in galaxies, in absence of a calibration fully independent of the current assumptions. Moreover, these results suggest that the use of a universal abundance at low and high redshift, and regardless of the galaxy population, can strongly bias the gas masses derived from [CI] $(M_{\rm H_2}([CI])$ scales as $([CI]/[H_2])^{-1})$, as in the case of the widespread [CI]/[H₂]= 3×10^{-5} value adopted in literature, following an estimate by Weiß et al. (2003) in a high-redshift QSO and the average abundance reported by Papadopoulos & Greve (2004). The ascertained redshift evolution of metallicity in galaxies and the complex and history of carbon production (e.g., Chiappini et al. 2003) argue against the use of universal abundance values, even if an early and quick enrichment might mitigate this issue in the cosmic ages explored so far.

5.2. The small fraction of atomic carbon in galaxies

A precise calibration of [C I] as a total gas tracer could be intrinsically difficult, since it requires the tracking of the small fraction of carbon produced in galaxies in the atomic gas phase. Neglecting the carbon locked into stars, the gas mass fraction of the neutral atomic carbon phase $f_{[C I]} = M_{[C I]}/M_{C}$ can be derived from the definition of the mass fraction of metals:

$$Z = \frac{M_{\text{metals}}}{M_{\text{H}_2}} = \frac{M_{\text{metals}}}{M_{\text{C}}} \frac{M_{\text{C}}}{M_{\text{[C I]}}} \frac{M_{\text{[C I]}}}{M_{\text{H}_2}}$$
(3)

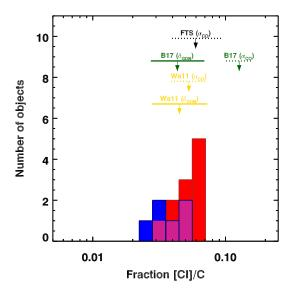


Figure 6. Atomic carbon fractions. The red and blue filled histograms show the distribution of the carbon fractions $f_{[\text{CI}]} = M_{[\text{CI}]}/M_{\text{C}}$ for our sample of MS galaxies with $> 3\sigma$ detections of $[\text{CI}](^3P_1 - ^3P_0)$ derived using a dustand CO(2-1)-based M_{H_2} , adopting $\delta_{\text{GDR}}(Z) = \delta_{\text{GDR}}(Z_{\odot})$ and $\alpha_{\text{CO}}(Z) = \alpha_{\text{CO}}(Z_{\odot})$. The colored segments and arrows show the mean $f_{[\text{CI}]}$ values and the standard deviation of the logarithmic distributions of SMGs and local LIRGs, as coded in the labels (B17: SPT-SMGs at $z \sim 4$, Wa11: SMGs at $z \sim 2.5$; FTS: Local LIRGs, no AGN).

where $M_{\rm C}$ is the total mass of carbon, $M_{\rm [C\,I]}$ the mass in the neutral atomic phase, $M_{\rm metals}$ the total mass of metals, and $M_{\rm H_2}$ is the hydrogen gas mass, excluding helium. From Eq. 3, we derive $f_{\rm [C\,I]} \propto \frac{M_{\rm [C\,I]}}{M_{\rm dust}\delta_{\rm GDR}/{\rm He}}$ or $\propto \frac{M_{\rm [C\,I]}}{L'_{\rm CO}\alpha_{\rm CO}/{\rm He}}.$ Assuming a solar metallicity and composition ($Z_{\odot}=0.0134$ and $\frac{M_{\rm C}}{M_{\rm metals}}=0.1779$, Asplund et al. 2009), the mass fraction of carbon in the atomic gas phase in the MS galaxies is $4.6^{+1.3}_{-1.0}\%$ and $3.4^{+1.4}_{-1.0}\%$ using M_{dust} and $L'_{\text{CO}(2-1)}$, respectively (Figure 6). These estimates and their uncertainties include upper limits through survival analysis and they represent the mean and standard deviation of the logarithmic distributions in Figure 6. Note that these values depend on the choice of metallicity and carbon fraction adopted here. Using the metallicity from the Fundamental Metallicity Relation does not impact this result (Section 4.4). We derive similar $f_{\rm [C\,I]}=6.0^{+3.3}_{-2.1}\%$ for LIRGs; $4.5^{+2.8}_{-1.7}\%$ and $5.3^{+1.9}_{-1.4}\%$ for SMGs at $z\sim2.5$ from W11/AZ13 using dust and CO respectively; $4.3^{+2.6}_{-1.6}\%$ and $12.7^{+3.2}_{-2.6}\%$ for SPT-SMGs from B17 adopting the dust- and CO-based calibration and including upper

limits. We used dust and CO to derive $M_{\rm gas}$, and assuming a metallicity of $Z\sim 2.8\,Z_{\odot}$ corresponding to $\alpha_{\rm CO}=0.8\,M_{\odot}/({\rm K~km~s^{-1}~pc^2})$ and $\delta_{\rm GDR}=30$. Supersolar metallicities are necessary to obtain these commonly adopted values when using the parametrization by Magdis et al. (2012b, their Eq. 8 with the corrected intercept discussed above and Section 4.2). However, while this likely has strong physical roots for the optically thin dust emission, $\alpha_{\rm CO}$ values of $\sim 0.8\,M_{\odot}/({\rm K~km~s^{-1}~pc^2})$ could be found also at $Z\sim Z_{\odot}$, being the CO emission optically thick and, thus, critically dependent on other parameters (i.e., the FWHM of the line).

The atomic carbon fractions $f_{[CI]}$ in Figure 6 reflect the similar $L'_{[C\,{\mbox{\scriptsize I}}]^3P_1\,-\,^3P_0}/L'_{{\rm CO}(2-1)}$ and $M_{[C\,{\mbox{\scriptsize I}}]}/M_{{
m dust}}$ ratios for MS and SBs/SMGs in Figure 4, analogously to the [CI] abundances shown in Figure 5. From a theoretical perspective, even simple plan-parallel PDR models could partially explain the observed constant $[CI](^3P_1 - ^3P_0)/CO(2-1)$ ratio by the relative insensitivity of the [CI] emission to the strength of UV radiation. In fact, while a stronger radiation field pushes the C-to-CO transition deeper into the gas slab, the size of the [CI]- and CO(2-1)-emitting regions stays relatively constant (e.g., Kaufman et al. 1999, and many others). Our $f_{[CI]}$ estimates suggest that [CI] represents a very minor fraction of the overall mass of carbon in galaxies, as the majority is in CO molecules (N([CI])/N(CO) = 0.1 - 0.2, Ikeda et al. 2002) and depleted on dust ($\sim 27\%$ of the overall carbon abundance, e.g., van Dishoeck & Black 1988), neglecting the quantity locked in stars. The small mass fraction of atomic carbon and the associated low column densities explain the small optical depth of the $[CI](^3P_1 - {}^3P_0)$ line, a major advantage in the use of this species to trace the gas content of galaxies (Papadopoulos et al. 2004). However, an accurate assessment of such minimal [CI] fractions and the detection of relative variations in different galaxy populations – if present – are complicated by both observational and theoretical uncertainties (e.g., the history of chemical enrichment in galaxies, affecting any tracers of the molecular gas mass other than H_2).

5.3. Possible hidden systematic variations of $[CI]/[H_2]$

We showed that MS and SB/SMGs have similar $L'_{[\text{CI}]^3P_1-{}^3P_0}/L'_{\text{CO}(2-1)}$ and $M_{[\text{CI}]}/M_{\text{dust}}$ ratios (Figure 4), resulting in different [CI]/[H₂] owing to standard assumptions on the dust/CO-to-gas conversion factors. However, reversing the argument, *intrinsic* large variations of [CI]/[H₂] might *not* directly translate into large differences in the observed ratios, due

to the counter-effect of higher $\delta_{\rm GDR}$ and $\alpha_{\rm CO}$ for MS galaxies than for SBs. Analogously, intrinsic systematic differences of [CI]/[H₂] between SB and MS would blur large variations of SFE into similar $L_{\rm IR}/L'_{\rm [C\,I]^3P_1\,-^3P_0}$ ratios, equivalently to what is observed for CO (Daddi et al. 2010b). The opposite dependence of $[CI]/[H_2]$ and $\delta_{\rm GDR}$ on metallicity could explain the small variations of $M_{\rm [C\,{\scriptscriptstyle I}]}/M_{\rm dust}$ observed in our data compilation: metal rich SB galaxies tend to have larger [CI]/[H₂] abundances than MS objects, compensating lower gasto-dust ratios $\delta_{\rm GDR}$. On the other hand, parameters other than metallicity should play a major role in the comparison of optically thick (CO) and thin ([CI], dust) tracers (e.g., turbulent velocities and compression resulting in broad CO lines, Bournaud et al. 2015). On top of these effects, enhanced cosmic ray rates in sources with large SFEs (e.g., Papadopoulos et al. 2004; Bisbas et al. 2015, 2017) could increase [CI]/[H₂], further reducing strong variations of the observed $M_{\rm [C\,{\scriptscriptstyle I}]}/M_{\rm dust}$ and $L'_{[C1]^3P_1-{}^3P_0}/L'_{CO(2-1)}$ ratios. The degeneracies listed here would be broken by an estimate of the gas mass independent of the assumptions we have to make for the currently available data.

6. CONCLUSIONS

We presented the first results of a survey targeting the $[CI](^3P_1 - ^3P_0)$ transition in main-sequence galaxies at $z \sim 1.2$, expanding the samples of starbursts and SMGs currently present in literature towards a population of normal galaxies.

We showed the existence of a sublinear correlation between the total $\log(L_{\rm IR})$ and $\log(L'_{\rm [C\,{\sc i}]^3}P_{1}\,{-\,}^3P_{0}),$ with a decreasing $L'_{[\text{C I}]^3P_1-{}^3P_0}/L_{\text{IR}}$ ratio with increasing L_{IR} . The slope of this relation and the $\sim 4\sigma$ significant displacement of the $[CI](^3P_1 - ^3P_0)$ -detected MS galaxies from the sequence traced by SBs/SMGs are similar to what is observed for CO (1-0). The difference will be easily tested by populating the distance from the mainsequence – $L'_{[C_1]^3P_1-{}^3P_0}/L_{IR}$ plane. Based on current evidence, starbursts may have lower values of this ratio than do main-sequence galaxies. These observations strengthen the [CI] – CO relation on global galaxy scales and suggest that $L'_{[C_I]^3P_1-{}^3P_0}/L_{IR}$ is an effective tracer of the depletion timescales in galaxies, decreasing with increasing $L_{\rm IR}$ and shorter in SBs/SMGs than in MS galaxies.

We further showed that the $L'_{[\text{C I}]^3P_1-{}^3P_0}/L'_{\text{CO}(2-1)}$ and $M_{[\text{C I}]}/M_{\text{dust}}$ ratios in local LIRGs, MS galaxies and SBs at $z \sim 1.2$, and lensed SMGs at z > 2.5-4 are similar, with an intrinsic scatter of ~ 0.2 dex. These ra-

tios are proportional to a mass fraction of carbon in the neutral atomic phase of $f_{\rm [C\,I]}=M_{\rm [C\,I]}/M_{\rm C}\sim 3-13\%$, roughly independent of the galaxy type and redshift, although affected by substantial scatter. The relative insensitivity of [C I] emission to the strength of the radiation field could partially explain the constant [C I](3P_1 – 3P_0)/CO (2 – 1) ratios, as the size of the [C I]- and CO-emitting regions stays relatively constant in different environments.

We then estimated the atomic carbon abundances - necessary to derive the total gas mass from [CI] observations – by comparing $[CI](^3P_1 - {}^3P_0)$, dust, and CO low-J emissions. Adopting standard $\alpha_{\rm CO}$ and gas-to-dust δ_{GDR} conversion factors, we find $[CI]/[H_2] \sim 1.6 - 1.9 \times 10^{-5}$ for MS galaxies at $z \sim 1.2$. These values are $\sim 3-8\times$ lower than the abundance in high-redshift SMGs, and $\sim 4 \times$ lower than in local LIRGs. At this stage, this difference is mainly a consequence of the choice of $\alpha_{\rm CO}$ and $\delta_{\rm GDR}$, and it currently exacerbates possible minimal differences in the observables, if present. However, systematically higher [CI]/[H₂] in SB than in MS galaxies, possibly driven by larger metallicities and/or cosmic rays rates, might result in similar observables, a degeneracy that cannot be broken with the available data and tools. All things considered, our findings caution against the use of a universal atomic carbon abundance regardless of the galaxy type and redshift.

ACKNOWLEDGEMENTS

We acknowledge the constructive comments from the anonymous referee, which significantly improved the content and presentation of the results. We thank Mark Sargent for providing the initial catalogs and discussions during the early stages of this work. FV and GEM acknowledge the Villum Fonden research grant 13160 "Gas to stars, stars to dust: tracing star formation across cosmic time" and the Cosmic Dawn Center of Excellence funded by the Danish National Research Foundation. YG acknowledges partial support of China grant no. 2017YFA0402704, NSFC grant no. 11420101002. This paper makes use of the following ALMA data: ADS/JAO.ALMA#2016.1.01040.S, #2015.1.00260.S, #2016.1.00171.S. ALMA is a partnership of ESO (representing its member states), NSF (USA) and NINS (Japan), together with NRC (Canada), MOST and ASIAA (Taiwan), and KASI (Republic of Korea), in cooperation with the Republic of Chile. The Joint ALMA Observatory is operated by ESO, AUI/NRAO and NAOJ. In this work we made use of the COSMOS master spectroscopic catalog, available within the collaboration and kept updated by Mara Salvato.

REFERENCES

Alaghband-Zadeh, S., Chapman, S. C., Swinbank, A. M., et al. 2012, MNRAS, 424, 2232, doi: 10.1111/j.1365-2966.2012.21386.x

—. 2013, MNRAS, 435, 1493, doi: 10.1093/mnras/stt1390

Aravena, M., Spilker, J. S., Bethermin, M., et al. 2016, MNRAS, 457, 4406, doi: 10.1093/mnras/stw275

Aretxaga, I., Wilson, G. W., Aguilar, E., et al. 2011, MNRAS, 415, 3831,

doi: 10.1111/j.1365-2966.2011.18989.x

Armus, L., Mazzarella, J. M., Evans, A. S., et al. 2009, PASP, 121, 559, doi: 10.1086/600092

Arnouts, S., Walcher, C. J., Le Fèvre, O., et al. 2007, A&A, 476, 137, doi: 10.1051/0004-6361:20077632

Asplund, M., Grevesse, N., Sauval, A. J., & Scott, P. 2009, ARA&A, 47, 481,

doi: 10.1146/annurev.astro.46.060407.145222

Bertoldi, F., Carilli, C., Aravena, M., et al. 2007, ApJS, 172, 132, doi: 10.1086/520511

Bisbas, T. G., Papadopoulos, P. P., & Viti, S. 2015, ApJ, 803, 37, doi: 10.1088/0004-637X/803/1/37

Bisbas, T. G., van Dishoeck, E. F., Papadopoulos, P. P., et al. 2017, ApJ, 839, 90, doi: 10.3847/1538-4357/aa696d

Bolatto, A. D., Wolfire, M., & Leroy, A. K. 2013, ARA&A, 51, 207, doi: 10.1146/annurev-astro-082812-140944

Bothwell, M. S., Smail, I., Chapman, S. C., et al. 2013, MNRAS, 429, 3047, doi: 10.1093/mnras/sts562

Bothwell, M. S., Aguirre, J. E., Aravena, M., et al. 2017, MNRAS, 466, 2825, doi: 10.1093/mnras/stw3270

Bournaud, F., Daddi, E., Weiß, A., et al. 2015, A&A, 575, A56, doi: 10.1051/0004-6361/201425078

Bruzual, G., & Charlot, S. 2003, MNRAS, 344, 1000, doi: 10.1046/j.1365-8711.2003.06897.x

Carilli, C. L., Menten, K. M., & Yun, M. S. 1999, ApJL, 521, L25, doi: 10.1086/312179

Carilli, C. L., & Walter, F. 2013, ARA&A, 51, 105, doi: 10.1146/annurev-astro-082812-140953

Casey, C. M., Narayanan, D., & Cooray, A. 2014, PhR, 541, 45, doi: 10.1016/j.physrep.2014.02.009

Casey, C. M., Berta, S., Béthermin, M., et al. 2012, ApJ, 761, 140, doi: 10.1088/0004-637X/761/2/140

- Catalano, A., Calvo, M., Ponthieu, N., et al. 2014, A&A, 569, A9, doi: 10.1051/0004-6361/201423557
- Chabrier, G. 2003, PASP, 115, 763, doi: 10.1086/376392
- Chiappini, C., Romano, D., & Matteucci, F. 2003, MNRAS, 339, 63, doi: 10.1046/j.1365-8711.2003.06154.x
- Cortzen, I., Garrett, J., Magdis, G., et al. 2018, ArXiv e-prints. https://arxiv.org/abs/1810.05178
- Cox, P., Krips, M., Neri, R., et al. 2011, ApJ, 740, 63, doi: 10.1088/0004-637X/740/2/63
- Daddi, E., Dickinson, M., Morrison, G., et al. 2007, ApJ, 670, 156, doi: 10.1086/521818
- Daddi, E., Bournaud, F., Walter, F., et al. 2010a, ApJ, 713, 686, doi: 10.1088/0004-637X/713/1/686
- Daddi, E., Elbaz, D., Walter, F., et al. 2010b, ApJL, 714, L118, doi: 10.1088/2041-8205/714/1/L118
- Daddi, E., Dannerbauer, H., Liu, D., et al. 2015, A&A, 577, A46, doi: 10.1051/0004-6361/201425043
- Draine, B. T., & Li, A. 2007, ApJ, 657, 810, doi: 10.1086/511055
- Efstathiou, A., & Siebenmorgen, R. 2009, A&A, 502, 541, doi: 10.1051/0004-6361/200811205
- Elbaz, D., Daddi, E., Le Borgne, D., et al. 2007, A&A, 468, 33, doi: 10.1051/0004-6361:20077525
- Frerking, M. A., Keene, J., Blake, G. A., & Phillips, T. G. 1989, ApJ, 344, 311, doi: 10.1086/167799
- Geach, J. E., Dunlop, J. S., Halpern, M., et al. 2017, MNRAS, 465, 1789, doi: 10.1093/mnras/stw2721
- Genzel, R., Tacconi, L. J., Gracia-Carpio, J., et al. 2010, MNRAS, 407, 2091,
 - doi: 10.1111/j.1365-2966.2010.16969.x
- Genzel, R., Tacconi, L. J., Lutz, D., et al. 2015, ApJ, 800, 20, doi: 10.1088/0004-637X/800/1/20
- Gerin, M., & Phillips, T. G. 2000, ApJ, 537, 644, doi: 10.1086/309072
- Glover, S. C. O., Clark, P. C., Micic, M., & Molina, F. 2015, MNRAS, 448, 1607, doi: 10.1093/mnras/stu2699
- Guilloteau, S., & Lucas, R. 2000, in Astronomical Society of the Pacific Conference Series, Vol. 217, Imaging at Radio through Submillimeter Wavelengths, ed. J. G. Mangum & S. J. E. Radford, 299
- Guilloteau, S., Omont, A., McMahon, R. G., Cox, P., & Petitjean, P. 1997, A&A, 328, L1
- Gullberg, B., Lehnert, M. D., De Breuck, C., et al. 2016, A&A, 591, A73, doi: 10.1051/0004-6361/201527647
- Ikeda, M., Oka, T., Tatematsu, K., Sekimoto, Y., & Yamamoto, S. 2002, ApJS, 139, 467, doi: 10.1086/338761
- Israel, F. P., Rosenberg, M. J. F., & van der Werf, P. 2015, A&A, 578, A95, doi: 10.1051/0004-6361/201425175

- Ivison, R. J., Papadopoulos, P. P., Smail, I., et al. 2011, MNRAS, 412, 1913, doi: 10.1111/j.1365-2966.2010.18028.x
- Ivison, R. J., Greve, T. R., Dunlop, J. S., et al. 2007, MNRAS, 380, 199, doi: 10.1111/j.1365-2966.2007.12044.x
- Ivison, R. J., Swinbank, A. M., Swinyard, B., et al. 2010, A&A, 518, L35, doi: 10.1051/0004-6361/201014548
- Jiao, Q., Zhao, Y., Zhu, M., et al. 2017, ApJL, 840, L18, doi: 10.3847/2041-8213/aa6f0f
- Jin, S., Daddi, E., Liu, D., et al. 2018, ApJ, 864, 56, doi: 10.3847/1538-4357/aad4af
- Juneau, S., Dickinson, M., Alexander, D. M., & Salim, S. 2011, ApJ, 736, 104, doi: 10.1088/0004-637X/736/2/104
- Kamenetzky, J., Rangwala, N., & Glenn, J. 2017, MNRAS, 471, 2917, doi: 10.1093/mnras/stx1595
- Kamenetzky, J., Rangwala, N., Glenn, J., Maloney, P. R., & Conley, A. 2016, ApJ, 829, 93, doi: 10.3847/0004-637X/829/2/93
- Kaplan, E. L., & Meier, P. 1958, J. Am. Stat. Assoc., 53, 282, doi: 10.2307/2281868
- Kaufman, M. J., Wolfire, M. G., Hollenbach, D. J., & Luhman, M. L. 1999, ApJ, 527, 795, doi: 10.1086/308102
- Keene, J., Lis, D. C., Phillips, T. G., & Schilke, P. 1996, in IAU Symposium, Vol. 178, Molecules in Astrophysics: Probes & Processes, ed. E. F. van Dishoeck, 129
- Kelly, B. C. 2007, ApJ, 665, 1489, doi: 10.1086/519947
 Kennicutt, Jr., R. C. 1998a, ARA&A, 36, 189, doi: 10.1146/annurev.astro.36.1.189
- —. 1998b, ApJ, 498, 541
- Kirkpatrick, A., Pope, A., Alexander, D. M., et al. 2012, ApJ, 759, 139, doi: 10.1088/0004-637X/759/2/139
- Kovács, A., Chapman, S. C., Dowell, C. D., et al. 2006, ApJ, 650, 592, doi: 10.1086/506341
- Kroupa, P. 2001, MNRAS, 322, 231, doi: 10.1046/j.1365-8711.2001.04022.x
- Laigle, C., McCracken, H. J., Ilbert, O., et al. 2016, ApJS, 224, 24, doi: 10.3847/0067-0049/224/2/24
- Lestrade, J.-F., Combes, F., Salomé, P., et al. 2010, A&A, 522, L4, doi: 10.1051/0004-6361/201015673
- Liu, D., Gao, Y., Isaak, K., et al. 2015, ApJL, 810, L14, doi: 10.1088/2041-8205/810/2/L14
- Liu, D., Daddi, E., Dickinson, M., et al. 2018, ApJ, 853, 172, doi: 10.3847/1538-4357/aaa600
- Lu, N., Zhao, Y., Díaz-Santos, T., et al. 2017, ApJS, 230, 1, doi: 10.3847/1538-4365/aa6476
- Lutz, D., Poglitsch, A., Altieri, B., et al. 2011, A&A, 532, A90, doi: 10.1051/0004-6361/201117107
- Ma, J., Gonzalez, A. H., Spilker, J. S., et al. 2015, ApJ, 812, 88, doi: 10.1088/0004-637X/812/1/88

- Magdis, G. E., Elbaz, D., Hwang, H. S., et al. 2010, MNRAS, 409, 22, doi: 10.1111/j.1365-2966.2010.17551.x
- Magdis, G. E., Daddi, E., Béthermin, M., et al. 2012a, ApJ, 760, 6, doi: 10.1088/0004-637X/760/1/6
- —. 2012b, ApJ, 760, 6, doi: 10.1088/0004-637X/760/1/6
- Magdis, G. E., Rigopoulou, D., Daddi, E., et al. 2017, A&A, 603, A93, doi: 10.1051/0004-6361/201731037
- Magnelli, B., Lutz, D., Santini, P., et al. 2012, A&A, 539, A155, doi: 10.1051/0004-6361/201118312
- Mannucci, F., Cresci, G., Maiolino, R., Marconi, A., & Gnerucci, A. 2010, MNRAS, 408, 2115, doi: 10.1111/j.1365-2966.2010.17291.x
- Maraston, C. 2005, MNRAS, 362, 799, doi: 10.1111/j.1365-2966.2005.09270.x
- Markwardt, C. B. 2009, in Astronomical Society of the Pacific Conference Series, Vol. 411, Astronomical Data Analysis Software and Systems XVIII, ed. D. A.
 Bohlender, D. Durand, & P. Dowler, 251
- McKean, J. P., Berciano Alba, A., Volino, F., et al. 2011, MNRAS, 414, L11, doi: 10.1111/j.1745-3933.2011.01043.x
- McMullin, J. P., Waters, B., Schiebel, D., Young, W., & Golap, K. 2007, in Astronomical Society of the Pacific Conference Series, Vol. 376, Astronomical Data Analysis Software and Systems XVI, ed. R. A. Shaw, F. Hill, & D. J. Bell, 127
- Menéndez-Delmestre, K., Blain, A. W., Smail, I., et al. 2009, ApJ, 699, 667, doi: 10.1088/0004-637X/699/1/667
- Mullaney, J. R., Alexander, D. M., Goulding, A. D., & Hickox, R. C. 2011, MNRAS, 414, 1082, doi: 10.1111/j.1365-2966.2011.18448.x
- Muzzin, A., Wilson, G., Demarco, R., et al. 2013, ApJ, 767, 39, doi: 10.1088/0004-637X/767/1/39
- Noeske, K. G., Weiner, B. J., Faber, S. M., et al. 2007, ApJL, 660, L43, doi: 10.1086/517926
- Ojha, R., Stark, A. A., Hsieh, H. H., et al. 2001, ApJ, 548, 253, doi: 10.1086/318693
- Oliver, S. J., Bock, J., Altieri, B., et al. 2012, MNRAS, 424, 1614, doi: 10.1111/j.1365-2966.2012.20912.x
- Ott, S. 2010, in Astronomical Society of the Pacific Conference Series, Vol. 434, Astronomical Data Analysis Software and Systems XIX, ed. Y. Mizumoto, K.-I. Morita, & M. Ohishi, 139
- Papadopoulos, P. P., & Greve, T. R. 2004, ApJL, 615, L29, doi: 10.1086/426059
- Papadopoulos, P. P., Thi, W.-F., & Viti, S. 2004, MNRAS, 351, 147, doi: 10.1111/j.1365-2966.2004.07762.x
- Popping, G., Decarli, R., Man, A. W. S., et al. 2017, A&A, 602, A11, doi: 10.1051/0004-6361/201730391

- Sanders, D. B., Mazzarella, J. M., Kim, D.-C., Surace, J. A., & Soifer, B. T. 2003, AJ, 126, 1607, doi: 10.1086/376841
- Sanders, D. B., Salvato, M., Aussel, H., et al. 2007, ApJS, 172, 86, doi: 10.1086/517885
- Sargent, M. T., Daddi, E., Béthermin, M., et al. 2014, ApJ, 793, 19, doi: 10.1088/0004-637X/793/1/19
- Schmidt, M. 1959, ApJ, 129, 243
- Scoville, N., Aussel, H., Brusa, M., et al. 2007, ApJS, 172, 1, doi: 10.1086/516585
- Scoville, N., Aussel, H., Sheth, K., et al. 2014, ApJ, 783, 84, doi: 10.1088/0004-637X/783/2/84
- Skrutskie, M. F., Cutri, R. M., Stiening, R., et al. 2006, AJ, 131, 1163, doi: 10.1086/498708
- Solomon, P. M., & Vanden Bout, P. A. 2005, ARA&A, 43, 677, doi: 10.1146/annurev.astro.43.051804.102221
- Stacey, H. R., McKean, J. P., Robertson, N. C., et al. 2018, MNRAS, 476, 5075, doi: 10.1093/mnras/sty458
- Stoerzer, H., Stutzki, J., & Sternberg, A. 1997, A&A, 323, L13
- Stutzki, J., Bensch, F., Heithausen, A., Ossenkopf, V., & Zielinsky, M. 1998, A&A, 336, 697
- Stutzki, J., Graf, U. U., Haas, S., et al. 1997, ApJL, 477, L33, doi: 10.1086/310514
- Swinbank, A. M., Smail, I., Longmore, S., et al. 2010, Nature, 464, 733, doi: 10.1038/nature08880
- Tacconi, L. J., Neri, R., Chapman, S. C., et al. 2006, ApJ, 640, 228, doi: 10.1086/499933
- Tacconi, L. J., Genzel, R., Saintonge, A., et al. 2018, ApJ, 853, 179, doi: 10.3847/1538-4357/aaa4b4
- U, V., Sanders, D. B., Mazzarella, J. M., et al. 2012, ApJS, 203, 9, doi: 10.1088/0067-0049/203/1/9
- van Dishoeck, E. F., & Black, J. H. 1988, ApJ, 334, 771, doi: 10.1086/166877
- Véron-Cetty, M.-P., & Véron, P. 2010, A&A, 518, A10, doi: 10.1051/0004-6361/201014188
- Vieira, J. D., Crawford, T. M., Switzer, E. R., et al. 2010, ApJ, 719, 763, doi: 10.1088/0004-637X/719/1/763
- Wagg, J., Carilli, C. L., Aravena, M., et al. 2014, ApJ, 783, 71, doi: 10.1088/0004-637X/783/2/71
- Walter, F., Weiß, A., Downes, D., Decarli, R., & Henkel, C. 2011, ApJ, 730, 18, doi: 10.1088/0004-637X/730/1/18
- Weiß, A., Downes, D., Henkel, C., & Walter, F. 2005, A&A, 429, L25, doi: 10.1051/0004-6361:200400085
- Weiß, A., Henkel, C., Downes, D., & Walter, F. 2003, A&A, 409, L41, doi: 10.1051/0004-6361:20031337
- Weiß, A., De Breuck, C., Marrone, D. P., et al. 2013, ApJ, 767, 88, doi: 10.1088/0004-637X/767/1/88
- Xie, T., Allen, M., & Langer, W. D. 1995, ApJ, 440, 674, doi: 10.1086/175305

Zanella, A., Daddi, E., Magdis, G., et al. 2018, MNRAS, 481, 1976, doi: 10.1093/mnras/sty2394

VALENTINO ET AL.

APPENDIX

A. GALAXY SPECTRAL ENERGY DISTRIBUTIONS AND SPECTRA

We show in Figure A.1 the 1D spectra of our sample of 21 galaxies at $z \sim 1.2$ observed with ALMA Band 6. The black line show the spectrum; the yellow area marks the channels used to measure the line fluxes, matching brighter CO lines, if present (Section 2.3, Table 1); the solid red line the best fitting Gaussian obtained fixing the redshift and width of the $[CI](^3P_1 - ^3P_0)$ line to match the brighter CO emissions and the continuum level to the estimate over the full 7.5 GHz band; the dashed dark red line shows the best $[CI](^3P_1 - ^3P_0)$ line model with free parameters for the line and a local continuum emission estimate within ± 2 GHz from the line center. When a line is not detected, we show in red the location of the expected $[CI](^3P_1 - ^3P_0)$ emission based on detected CO lines. The black thick shows the expected position of the line based on the optical/near-infrared spectroscopic redshift. Figure A.1 further shows the near-infrared to radio photometry for our sample. The filled red circles mark the data points we considered for our modeling (black line). The empty red circles were not considered in the fit (Magdis et al. 2012b). Arrows mark 3σ upper limits. The solid blue line shows the best fit template for the dusty torus component.

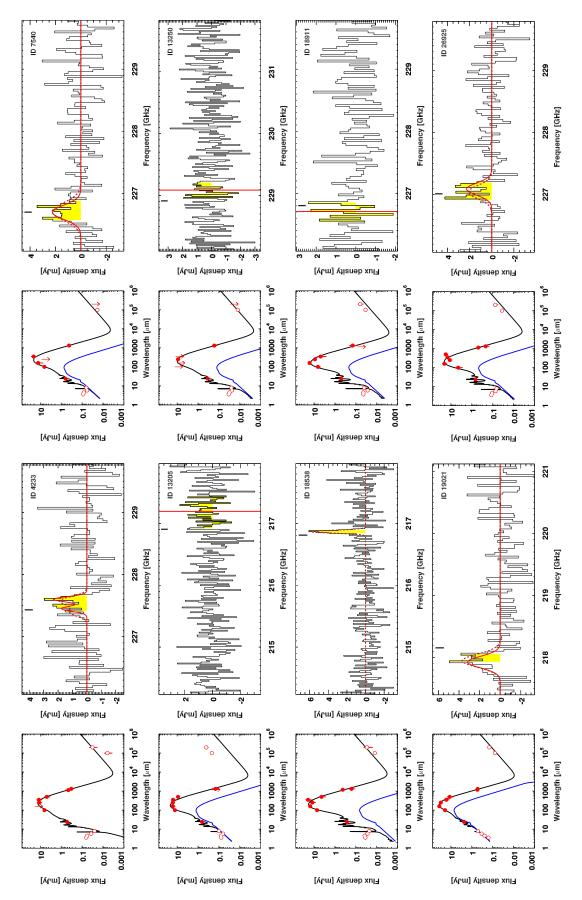


Figure A.1. Far infrared SEDs and $[CI](^3P_1 - ^3P_0)$ spectra of our sample of 21 galaxies at $z \sim 1.2$ followed up with ALMA.

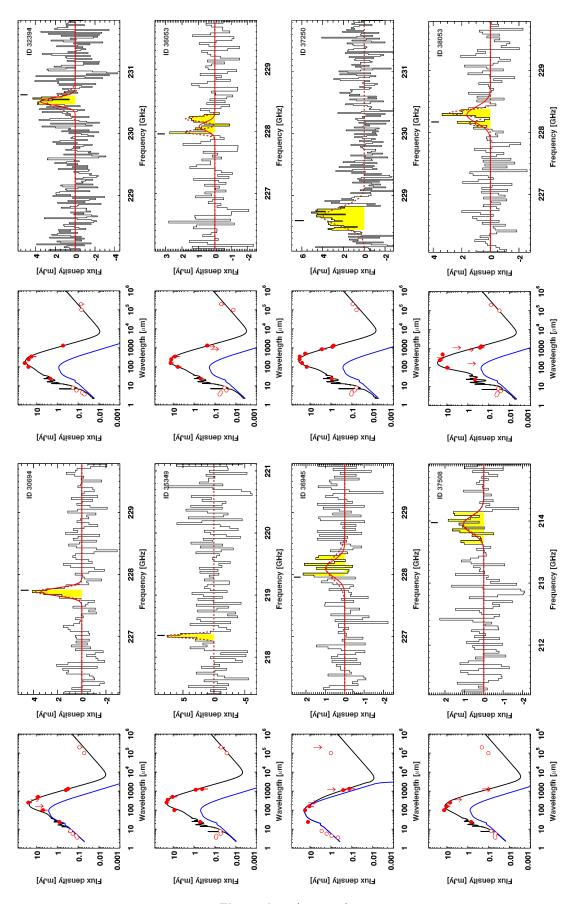


Figure A.1. (continue)

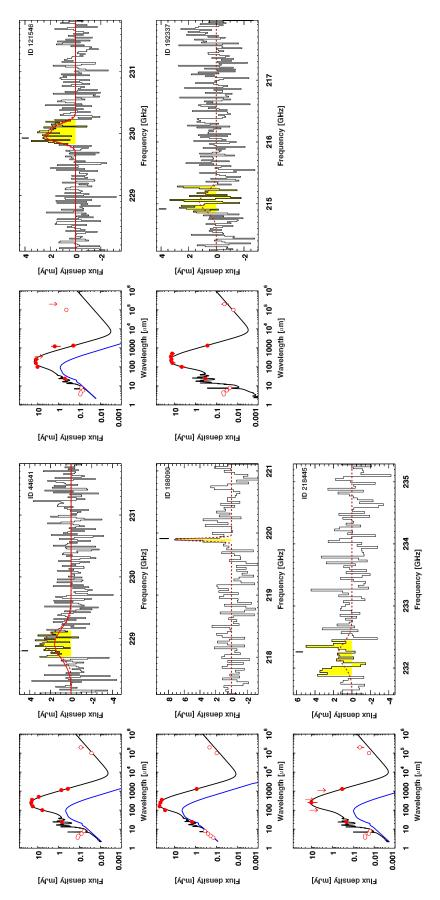


Figure A.1. (continue)

Table 1. Main-sequence galaxies at $z \sim 1.2$.

RA Decl z _{spec}		zspe	30	$\log(M_{\star})$	$L_{ m IR}$	$L_{ m FIR}$	$L'_{[CI]}{}^3P_1 - {}^3P_0$	$L'_{\mathrm{CO}(2-1)}$	$I_{[\operatorname{C} \operatorname{I}]^3P_1-^3P_0}$	$I_{\text{CO}(2-1)}$	$f_{ m AGN}$	Type
(deg) (deg) M_{\odot} $10^{11} L_{\odot}$	M_{\odot}			$10^{11}L_{\odot}$		$10^{11}L_{\odot}$	$10^{10} \text{ K km s}^{-1} \text{ pc}^2$	$10^{10} \text{ K km s}^{-1} \text{ pc}^2$	$\rm Jy~km~s^{-1}$	$\rm Jy\;km\;s^{-1}$		
(2) (3) (4) (5) (6)	(5)	(5)	(5) (6)	(9)		(7)	(8)	(6)	(10)	(11)	(12)	(13)
150.39732 2.24088 1.1630 ± 0.0003^{a} 10.89 8.09 ± 0.49	$1.1630 \pm 0.0003^{\mathrm{a}}$ 10.89	10.89	89	8.09 ± 0.4	63	5.05 ± 0.30	0.24 ± 0.05	1	0.6 ± 0.14	1	1	MS
$[50.41281 1.85157 1.1714 \pm 0.0003^{a} 11.06 9.36 \pm 1.32$	1.1714 ± 0.0003^{a} 11.06	11.06	90	9.36 ± 1.3	22	7.36 ± 1.04	0.34 ± 0.08	I	0.86 ± 0.19	I	0.12	$_{ m MS}$
$150.57484 1.94786 1.2660 \pm 0.0004^{\rm b} 11.10 12.28 \pm 1.27$	$1.2660 \pm 0.0004^{\rm b}$ 11.10	11.10		$12.28 \pm 1.$	27	9.68 ± 1.00	< 0.2	1.93 ± 0.39	< 0.44	0.92 ± 0.18	0.16	\overline{MS}
$(50.17650 1.95523 1.1484 \pm 0.0002^{a} 10.41 5.22 \pm 1.54$	1.1484 ± 0.0002^{a} 10.41	10.41		5.22 ± 1.8	54	3.68 ± 1.09	< 0.1	I	< 0.26	I	0.04	$_{ m MS}$
$150.12639 2.43285 1.2694 \pm 0.0001^{\circ} 10.56 9.83 \pm 9.45$	$1.2694 \pm 0.0001^{\circ}$ 10.56	10.56		9.83 ± 9.4	5	8.22 ± 7.91	0.19 ± 0.02	I	0.41 ± 0.05	I	0.01	$_{ m MS}$
150.04820 2.46767 1.1709 ± 0.0003^{a} 10.64 7.78 ± 1.68	$1.1709 \pm 0.0003^{\mathrm{a}}$ 10.64	10.64		7.78 ± 1.6	_∞	5.87 ± 1.27	< 0.16	0.58 ± 0.13	< 0.39	0.32 ± 0.07	0.04	\overline{MS}
$150.05878 2.47739 1.2581 \pm 0.0003^{d} 11.78 19.27 \pm 1.57$	$1.2581 \pm 0.0003^{\rm d}$ 11.78	11.78		19.27 ± 1.8	22	14.57 ± 1.19	0.35 ± 0.07	1.90 ± 0.24	0.76 ± 0.14	0.91 ± 0.11	0.41	AGN
$150.46350 1.88331 1.1671 \pm 0.0003^{a} 11.05 9.13 \pm 1.66$	$1.1671 \pm 0.0003^{\mathrm{a}}$ 11.05	11.05		9.13 ± 1.6	9	7.56 ± 1.37	0.35 ± 0.06	1.47 ± 0.22	0.88 ± 0.16	0.81 ± 0.12	0.08	$_{ m MS}$
149.66026 2.41099 1.1606 ± 0.0002^a 10.78 8.67 ± 1.45	$1.1606 \pm 0.0002^{\mathrm{a}}$ 10.78	10.78		8.67 ± 1.4	15	7.58 ± 1.26	0.24 ± 0.03	1.62 ± 0.21	0.61 ± 0.09	0.91 ± 0.12	0.32	MS
$150.06781 1.85108 1.1345 \pm 0.0001^{a} 10.03 22.54 \pm 6.37$	$1.1345 \pm 0.0001^{\mathrm{a}}$ 10.03	10.03		22.54 ± 6 .	37	12.90 ± 3.65	0.24 ± 0.05	I	0.64 ± 0.12	I	90.0	$_{\mathrm{SB}}$
$150.49902 1.72446 1.2543 \pm 0.0002^{c} 11.19 11.5 \pm 1.83$	1.2543 ± 0.0002^{c} 11.19	11.19		$11.5 \pm 1.$	83	8.65 ± 1.38	0.41 ± 0.11	3.57 ± 0.44	0.89 ± 0.25	1.72 ± 0.21	0.07	$\overline{\mathrm{MS}}$
149.68564 1.91986 1.1573 ± 0.0003^{a} 10.87 7.69 ± 3.24	$1.1573 \pm 0.0003^{\mathrm{a}}$ 10.87	10.87		7.69 ± 3	24	5.38 ± 2.26	0.17 ± 0.05	I	0.43 ± 0.13	I	0.04	\overline{MS}
$150.19550 2.12404 1.1569 \pm 0.0003^{a} 11.43 0.44 \pm 0.03$	1.1569 ± 0.0003^{a} 11.43	11.43		0.44 ± 0.0	03	0.37 ± 0.02	0.17 ± 0.05	1.31 ± 0.37	0.44 ± 0.14	0.47 ± 0.13	0.99	AGN
$149.61813 2.19346 1.1526 \pm 0.0002^{\circ} 10.96 16.21 \pm 6.97$	$1.1526 \pm 0.0002^{\circ}$ 10.96	10.96		16.21 ± 6	26.	12.48 ± 5.37	0.68 ± 0.06	4.58 ± 0.32	1.76 ± 0.16	2.6 ± 0.18	0.03	\overline{MS}
$150.38953 2.25585 1.3020 \pm 0.0003^{\rm b} 11.04 11.20 \pm 2.17$	$1.3020 \pm 0.0003^{\rm b}$ 11.04	11.04	04	11.20 ± 2	.17	6.38 ± 1.24	0.31 ± 0.08	1.48 ± 0.42	0.64 ± 0.16	0.43 ± 0.12	0.12	\overline{MS}
$150.55685 2.39140 1.1562 \pm 0.0003^{a} 10.66 12.90 \pm 4.03$	1.1562 ± 0.0003^{a} 10.66	10.66		12.90 ± 4 .	03	10.84 ± 3.38	0.26 ± 0.05	1.69 ± 0.31	0.67 ± 0.14	0.96 ± 0.17	0.03	$_{\mathrm{SB}}$
150.65852 2.31786 1.1495 ± 0.0002^a 11.10 9.19 ± 1.99	1.1495 ± 0.0002^{a} 11.10	11.10	10	9.19 ± 1.9	6	7.72 ± 1.67	0.44 ± 0.06	1.63 ± 0.35	1.16 ± 0.17	0.93 ± 0.20	0.07	$_{ m MS}$
$150.05910 2.21995 1.1392 \pm 0.0002^{a} 11.08 6.89 \pm 0.94$	1.1392 ± 0.0002^{a} 11.08	11.08	80	6.89 ± 0.9	4	5.28 ± 0.72	0.39 ± 0.04	I	1.04 ± 0.12	I	0.16	$_{ m MS}$
$150.42799 2.55860 1.2383 \pm 0.0002^{\circ}$ 11.12 28.97 ± 1.22	$1.2383 \pm 0.0002^{\circ}$ 11.12	11.12		28.97 ± 1	1.22	22.74 ± 0.96	0.23 ± 0.04	I	0.51 ± 0.09	I	0.22	$^{\mathrm{SB}}$
$150.42073 2.62297 1.2884 \pm 0.0003^{\circ} 10.90 9.06 \pm 0.64$	$1.2884 \pm 0.0003^{\circ}$ 10.90	10.90	06	$9.06 \pm 0.$	64	7.50 ± 0.53	0.30 ± 0.07	I	0.62 ± 0.14	I	I	\overline{MS}
149.92007 2.61905 1.1199 \pm 0.0004° 10.60 3.83 \pm 2.19	1.1199 ± 0.0004^{c} 10.60	10.60		$3.83 \pm 2.$	61	3.25 ± 1.86	0.49 ± 0.09	I	1.33 ± 0.25	I	0.04	MS

Note—1- ID; 2, 3 - RA, Decl J2000; 4 - Spectroscopic redshift from sub-millimeter emission lines: a: From CO (4-3); b: CO (5-4); c: [C $[(^3P_1-^3P_0)$; d: CO (2-1); 5 - Stellar mass from SED modeling (Muzzin et al. 2013; Laigle et al. 2016). Uncertainty: 0.2 dex; 6 - Total infrared luminosity integrated within 8 - 1000 μ m due to star formation (i.e., corrected for torus emission); 7 - Far-infrared luminosity integrated within 40 - 400 μ m due to star formation (i.e., corrected for torus emission); 8, 9 - Galaxy-integrated $L'_{[C1]^3P_1-3P_0}$ and $L'_{CO(2-1)}$; 10, 11 - Galaxy velocity integrated [C I]($^3P_1-^3P_0$) and CO (2-1) fluxes. These estimates are obtained as weighted average flux densities within the channels maximizing the SNR of the lines, times the velocity width covered by these channels, and a 10% correction to total fluxes from the comparison with the best Gaussian modeling with all free parameters; 12 - Fraction of infrared AGN emission: $L_{AGN+SF} = L_{IR}/(1-f_{AGN})$; 13 - Galaxy type: MS = main-sequence; SB = Starburst (> 3.5× above the main-sequence); AGN = SED dominated by torus emission.

 † : selected based on $z_{\rm opt/NIR}$ from Casey et al. (2012). Upper limits are at $3\sigma.$

	Table 2	. Main-s	sequenc	ce galaxies a	t $z \sim 1.2$ (continu	e).
ID	$M_{ m dust}$	$\delta_{ m GDR}$	α_{CO}	$M_{ m [C{\scriptscriptstyle I}]}$	$[CI]/[H_2]_{(dust)}$	$[\mathrm{CI}]/[\mathrm{H_2}]_{(\mathrm{CO})}$
	$10^8 M_{\odot}$			$10^6 M_{\odot}$	$\times 10^{-5}$	$\times 10^{-5}$
(1)	(2)	(3)	(4)	(5)	(6)	(7)
4233	5.8 ± 1.1	82.0	_	3.0 ± 0.7	1.4 ± 0.8	_
7540	7.7 ± 1.2	72.5	_	4.3 ± 0.9	1.7 ± 0.9	_
13205	$2.3\pm0.3^*$	72.3	2.6	< 2.5	< 3.4	< 1.0
13250	2.6 ± 0.7	121.5	_	< 1.3	< 0.9	_
18538	3.5 ± 0.5	114.3	_	2.4 ± 0.3	1.4 ± 0.7	_
18911	$1.2\pm0.2^*$	102.5	4.2	< 1.9	< 3.7	< 1.5
19021	5.7 ± 0.5	76.3	2.8	4.3 ± 0.8	2.3 ± 1.1	1.6 ± 0.8
26925	4.6 ± 0.7	72.8	2.6	4.4 ± 0.8	2.9 ± 1.5	2.2 ± 1.1
30694	4.2 ± 0.4	91.2	3.6	3.0 ± 0.4	1.8 ± 0.9	1.0 ± 0.5
32394	7.6 ± 1.6	30.0	_	3.0 ± 0.6	3.0 ± 1.6	_
35349	12.0 ± 2.8	76.3	2.8	5.1 ± 1.4	1.3 ± 0.7	1.0 ± 0.5
36053	3.2 ± 0.7	82.9	_	2.1 ± 0.6	1.8 ± 1.1	_

Table 2. Main-sequence galaxies at $z \sim 1.2$ (continue)

No continuum detection in the Rayleigh-Jeans tail of the dust emission. This value should be treated as an order of magnitude estimate.

 2.2 ± 0.7

 8.5 ± 0.8

 3.9 ± 1.0

 3.3 ± 0.7

 5.5 ± 0.8

 4.9 ± 0.6

 2.8 ± 0.5

 3.7 ± 0.8

 6.1 ± 1.1

 1.6 ± 0.9

 2.4 ± 1.1

 12.6 ± 6.6

 8.0 ± 4.2

 2.6 ± 1.3

 6.0 ± 3.2

 2.6 ± 1.3

 2.2 ± 1.2 2.2 ± 1.2 1.1 ± 0.7

 1.1 ± 0.5

 1.8 ± 1.1

 4.6 ± 2.5

 2.6 ± 1.4

 4.0 ± 0.7

 9.6 ± 0.8

 $0.9 \pm 0.1^*$

 3.1 ± 0.4

 7.0 ± 0.7

 $2.7 \pm 0.7^{\dagger}$

 8.4 ± 0.8

 4.6 ± 0.6

 6.4 ± 1.7

76.3

83.9

75.1

30.0

70.2

69.1

30.0

82.4

97.0

2.8

3.2

2.7

0.8

2.5

36945

37250

37508

38053

44641

121546

188090

192337

218445

NOTE—1 - ID; 2 - Dust mass from SED modeling; 3 - Gas-to-dust conversion factor. Value fixed to $\delta_{\rm GDR}=30$ for starbursts. Uncertainty: 0.2 dex; 4 - $\alpha_{\rm CO}$ conversion factor. Value fixed to $\alpha_{\rm CO}=0.8~M_{\odot}/({\rm K~km~s^{-1}~pc^2})$ for starbursts. Uncertainty: 0.2 dex; 5 - Mass of [C I] (from $L'_{\rm [C\,I]^3P_1-^3P_0}$ assuming $T_{\rm ex}=30~{\rm K}$); 6 - Atomic carbon abundance adopting $M_{\rm gas}({\rm dust})$ and removing the 1.36× contribution of helium; 7 - Atomic carbon abundance adopting $M_{\rm gas}({\rm CO})$ and removing the 1.36× contribution of helium.

Upper limits are $< 3\sigma$. Systematic uncertainties on $M_{\rm gas}$ are not included in the error budget.

Significant blending of the photometry.

Table 3. Local galaxies.

Ð	$D_{ m \Gamma}$	zsbec	$\log(M_{\star})$	$L_{ m IR}$	$L'_{[CI]^3P_1-^3P_0}$	$L'_{\mathrm{CO}(1-0)}$	$L'_{\mathrm{CO}(2-1)}$	$^{I}_{[\text{C I}]^3P_1-^3P_0}$	$I_{\text{CO}(1-0)}$	$I_{\mathrm{CO}(2-1)}$	$^{\eta}$ beam	AGN
	Мрс		M_{\odot}	$_{10^{11}~L_{\odot}}$	$10^8~{\rm K~km~s^{-1}~pc^2}$	$10^8~\mathrm{K~km~s}^{-1}~\mathrm{pc}^2$	$10^8~\mathrm{K~km~s^{-1}~pc^2}$	$_{10^2~\mathrm{Jy~km~s}^{-1}}$	10^2 Jy km s $^{-1}$	10^2 Jy km s $^{-1}$		
(1)	(2)	(3)	(4)	(5)	(9)	(2)	(8)	(6)	(10)	(11)	(12)	(13)
Arp193	101.6	0.02330	10.5	4.8 ± 1.0	10.4 ± 3.3	39.4 ± 4.2	35.3 ± 5.5	7.7 ± 2.4	1.6 ± 0.2	5.7 ± 0.9	1	z
Arp220	78.7	0.01813	10.7	16.4 ± 3.3	13.8 ± 2.8	81.0 ± 4.5	77.9 ± 15.7	16.9 ± 3.4	5.4 ± 0.3	20.9 ± 4.2	1.21	>
Arp299-A	44.9	0.01041	I	2.9 ± 0.6	4.8 ± 1.2	28.4 ± 3.2	30.1 ± 2.4	17.8 ± 4.3	5.8 ± 0.7	24.6 ± 1.9	1.37	Z
Arp299-B	44.9	0.01041	I	1.6 ± 0.3	7.3 ± 2.1	18.8 ± 2.2	26.7 ± 2.5	27.2 ± 7.9	3.8 ± 0.4	21.8 ± 2.1	1.29	Z
Arp299-C	44.9	0.01041	ı	1.4 ± 0.3	6.8 ± 1.6	17.7 ± 2.1	21.8 ± 2.2	25.2 ± 6.0	3.6 ± 0.4	17.8 ± 1.8	1.26	z
CGCG049-057	56.2	0.01300	8.6	1.8 ± 0.4	2.3 ± 0.7	ı	ı	5.5 ± 1.6	ı	I	ı	z
ESO173-G015	42.0	0.00974	10.4	3.7 ± 0.7	7.1 ± 1.5	ı	ı	30.1 ± 6.4	I	I	1.88	z
IRASF18293-3413	78.9	0.01818	10.9	6.1 ± 1.2	20.9 ± 2.6	118.6 ± 11.0	78.9 ± 8.0	25.4 ± 3.2	7.9 ± 0.7	21.1 ± 2.1	1.10	z
M82	3.4	0.00094	10.0	0.4 ± 0.1	0.5 ± 0.1	4.0 ± 0.3	3.8 ± 0.3	352.8 ± 53.5	140.5 ± 9.9	537.2 ± 41.2	2.08	z
MCG+12-02-001	68.0	0.01570	I	2.6 ± 0.5	4.1 ± 1.1	49.0 ± 9.8	52.9 ± 8.0	6.7 ± 1.8	4.4 ± 0.9	19.0 ± 2.9	1.53	Z
Mrk331	80.3	0.01848	10.7	3.0 ± 0.6	7.3 ± 1.6	31.1 ± 5.4	22.3 ± 3.4	8.6 ± 1.9	2.0 ± 0.3	5.8 ± 0.9	1	z
NGC0253	3.4	0.00081	10.4	0.3 ± 0.1	0.9 ± 0.1	5.5 ± 0.4	5.1 ± 0.4	570.8 ± 76.2	191.6 ± 13.3	711.1 ± 52.8	2.19	7
NGC1068	16.1	0.00379	11.0	1.3 ± 0.3	5.6 ± 0.4	36.2 ± 4.7	33.8 ± 3.2	161.0 ± 11.8	57.3 ± 7.5	214.1 ± 20.3	1.87	7
NGC1365-NE	23.1	0.00546	I	1.4 ± 0.3	5.3 ± 0.6	48.0 ± 1.2	24.1 ± 3.9	73.8 ± 8.6	37.0 ± 0.9	74.1 ± 12.0	1.76	>
NGC1365-SW	23.1	0.00546	ı	1.4 ± 0.3	7.3 ± 0.7	74.3 ± 1.7	29.6 ± 4.8	103.1 ± 10.5	57.3 ± 1.3	91.2 ± 14.8	2.79	7
NGC3256	40.4	0.00935	10.8	4.2 ± 0.8	9.2 ± 1.1	56.6 ± 5.4	128.9 ± 13.3	42.7 ± 4.9	14.3 ± 1.4	130.7 ± 13.5	1.29	Z
NGC5135	59.3	0.01369	10.9	1.8 ± 0.4	9.3 ± 1.1	40.6 ± 3.7	1	20.0 ± 2.3	4.8 ± 0.4	ı	1.11	>
NGC6240	106.8	0.02448	11.4	6.8 ± 1.4	25.3 ± 5.0	79.3 ± 8.1	149.1 ± 29.9	16.9 ± 3.4	2.9 ± 0.3	21.9 ± 4.4	1	¥
NGC7469	8.02	0.01632	11.1	3.5 ± 0.7	10.5 ± 1.8	41.4 ± 3.4	101.3 ± 15.6	15.9 ± 2.7	3.4 ± 0.3	33.6 ± 5.2	1.22	¥
NGC7552	22.8	0.00536	10.5	1.0 ± 0.2	2.6 ± 0.4	13.0 ± 0.9	17.2 ± 1.7	37.8 ± 6.3	10.3 ± 0.8	54.5 ± 5.5	1.45	Z
NGC7582	22.3	0.00525	10.6	0.7 ± 0.1	2.7 ± 0.4	14.7 ± 1.1	21.6 ± 2.3	41.2 ± 6.1	12.2 ± 0.9	71.4 ± 7.6	1.87	¥
NGC7771	61.8	0.01427	11.2	2.4 ± 0.5	8.5 ± 1.1	67.9 ± 5.3	77.9 ± 11.7	16.8 ± 2.1	7.4 ± 0.6	33.9 ± 5.1	1.68	Z
VV340A	147.9	0.03367	11.2	5.3 ± 1.1	33.6 ± 8.9	108.6 ± 17.4	I	11.8 ± 3.1	2.1 ± 0.3	Ι	1.08	z
CenA	7.7	0.00183	11.1	0.4 ± 0.1	3.1 ± 0.2	21.0 ± 2.1	10.6 ± 1.5	392.1 ± 26.2	144.5 ± 14.8	291.1 ± 41.2	9.80	>
IC1623	87.3	0.02007	ļ	4.7 ± 0.9	15.4 ± 2.7	52.6 ± 5.8	77.6 ± 11.8	15.4 ± 2.7	2.9 ± 0.3	17.0 ± 2.6		Z
NGC0034	85.3	0.01962	10.7	3.2 ± 0.6	5.1 ± 1.5	24.9 ± 2.4	13.8 ± 2.8	5.4 ± 1.5	1.4 ± 0.1	3.2 ± 0.7	1.07	>
NGC0891-North	7.4	0.00176	I	0.14 ± 0.03	0.8 ± 0.2	6.4 ± 1.0	6.9 ± 1.0	107.5 ± 20.7	47.9 ± 7.3	207.8 ± 31.2	4.88	z
NGC0891-South	7.4	0.00176	ı	0.13 ± 0.03	1.7 ± 0.3	ı	I	230.4 ± 42.3	Ι	Ι	I	z
NGC2146-NUC	12.6	0.00298	I	0.6 ± 0.1	0.9 ± 0.1	7.1 ± 0.2	7.7 ± 0.7	42.9 ± 6.8	18.4 ± 0.6	79.3 ± 7.2	1.65	Z
NGC2146-NW	12.6	0.00298	I	0.6 ± 0.1	1.2 ± 0.2	7.5 ± 0.2	8.9 ± 0.8	55.8 ± 7.1	19.4 ± 0.6	91.4 ± 8.4	1.69	Z
NGC2146-SE	12.6	0.00298	I	0.6 ± 0.1	1.1 ± 0.1	7.8 ± 0.2	8.1 ± 1.6	49.4 ± 6.9	20.2 ± 0.6	83.8 ± 16.8	1.76	z
NGC3227	16.3	0.00386	10.2	0.07 ± 0.01	0.9 ± 0.2	5.8 ± 0.6	I	25.0 ± 6.7	9.0 ± 1.0	1	2.27	Y

Nore—1 - ID; 2 - Distance; 3 - Redshift; 4 - Stellar mass from 2MASS K_s -band photometry (Chabrier 2003 IMF, uncertainty ~ 0.2 dex); 5 - Total infrared luminosity integrated within 8 - 1000 μ m: $L_{IR} = L_{FIR}(40 - 400 \mu$ m) $\times 1.2$; 6 - 8: $L'_{[C1]^3P_1 - 3P_0}$, $L'_{CO(1-0)}$, $L'_{CO(2-1)}$; 9 - Galaxy integrated [C1]($^3P_1 - ^3P_0$) velocity integrated flux from FTS observations (Liu et al. 2015); 10, 11 - Galaxy integrated CO(1 - 0) and CO(2 - 1) fluxes from ground-based facilities. These values are signal-to-noise weighted means of all the available measurements in a fixed beam of 43.5" as in Table 3 of Kamenetzky et al. (2016), corrected by the beam factor in column (12); 12 - Beam correction for low-J CO fluxes in columns (10, 11): $\eta_{\text{beam}} = I_{[C1]}(\text{L15}, \text{total})/I_{[C1]}(\text{K16}, 43.5" beam)$; 13 - Active galactic nuclei entry in Véron-Cetty & Véron (2010): Y(es)/N(o).

References: Cols 5, 9: Liu et al. (2015), this work; Cols 10, 11: Kamenetzky et al. (2016); Col 13: Véron-Cetty & Véron (2010).

Table 4. Local galaxies (continue).

	M	M (CO)	[0]/[II]
ID	$M_{ m [C{\scriptscriptstyle I}]}$		$[\mathrm{C}\mathrm{I}]/[\mathrm{H}_2]_{(\mathrm{CO})}$
	$10^5~M_{\odot}$	$10^9~M_{\odot}$	$\times 10^{-5}$
(1)	(2)	(3)	(4)
Arp193	13.0 ± 4.1	3.2 ± 1.5	9.3 ± 5.3
Arp220	17.3 ± 3.5	6.5 ± 3.0	6.0 ± 3.1
Arp299-A	6.0 ± 1.5	2.3 ± 1.1	6.0 ± 3.2
Arp299-B	9.1 ± 2.7	1.5 ± 0.7	13.7 ± 7.7
Arp299-C	8.4 ± 2.0	1.4 ± 0.7	13.5 ± 7.2
CGCG049-057	2.9 ± 0.8	_	_
ESO173-G015	8.8 ± 1.9	_	_
IRASF18293-3413	26.0 ± 3.3	9.5 ± 4.5	6.2 ± 3.0
M82	0.7 ± 0.1	0.3 ± 0.1	4.9 ± 2.4
MCG+12-02-001	5.1 ± 1.3	3.9 ± 2.0	3.0 ± 1.7
Mrk331	9.2 ± 2.0	2.5 ± 1.2	8.4 ± 4.5
NGC0253	1.1 ± 0.1	0.4 ± 0.2	5.8 ± 2.8
NGC1068	7.0 ± 0.5	2.9 ± 1.4	5.4 ± 2.6
NGC1365-NE	6.6 ± 0.8	3.8 ± 1.8	3.9 ± 1.8
NGC1365-SW	9.2 ± 0.9	5.9 ± 2.7	3.5 ± 1.7
NGC3256	11.5 ± 1.3	4.5 ± 2.1	5.8 ± 2.8
NGC5135	11.6 ± 1.3	3.2 ± 1.5	8.1 ± 3.9
NGC6240	31.6 ± 6.3	6.3 ± 3.0	11.3 ± 5.8
NGC7469	13.1 ± 2.3	3.3 ± 1.5	9.0 ± 4.5
NGC7552	3.3 ± 0.5	1.0 ± 0.5	7.1 ± 3.5
NGC7582	3.4 ± 0.5	1.2 ± 0.6	6.6 ± 3.2
NGC7771	10.6 ± 1.3	5.4 ± 2.5	4.4 ± 2.1
VV340A	42.0 ± 11.1	8.7 ± 4.2	10.9 ± 6.1
CenA	3.9 ± 0.3	1.7 ± 0.8	5.3 ± 2.5
IC1623	19.2 ± 3.3	4.2 ± 2.0	10.4 ± 5.2
NGC0034	6.4 ± 1.8	2.0 ± 0.9	7.3 ± 4.0
NGC0891-North	1.0 ± 0.2	0.5 ± 0.2	4.4 ± 2.3
NGC0891-South	2.1 ± 0.4	_	_
NGC2146-NUC	1.1 ± 0.2	0.6 ± 0.3	4.5 ± 2.2
NGC2146-NW	1.5 ± 0.2	0.6 ± 0.3	5.6 ± 2.7
NGC2146-SE	1.3 ± 0.2	0.6 ± 0.3	4.7 ± 2.3
NGC3227	1.1 ± 0.3	0.5 ± 0.2	5.4 ± 2.9

NOTE—1 - ID; 2 - Mass of [C I] (from $L'_{[{\rm C\,I}]^3P_1\,-\,^3P_0}$ assuming $T_{\rm ex}=30$ K); 3 - Gas mass from CO (1 - 0), assuming $\alpha_{CO}=0.8~M_{\odot}/({\rm K~km~s^{-1}~pc^2})$ (with an uncertainty of 0.2 dex); 4 - Atomic carbon abundance adopting $M_{\rm gas}({\rm CO})$ and removing the 1.36× contribution of helium.

Table 5. Sub-millimeter galaxies and QSOs at $z \gtrsim 2.5$.

7 20	$\mu_{ m grav}$	$L_{ m IR}$	$L_{ m FIR}$	$L'_{[CI]}{}^3P_1 - {}^3P_0$	$L'_{\mathrm{CO}(3-2)}$	I [CI] $^{3}P_{1}-^{3}P_{0}$	$^{I_{\rm CO(3-2)}}$	$M_{ m dust}$	$M_{ m [C\ I]}$	[C I] [H2] dust	$\frac{[CI]}{[H_2]}_{CO}$	$f_{ m AGN}$	QSOs
$_{10^{12}~L_{\odot}}$	012 $_{L_{\odot}}$		$_{10^{12}~L_{\odot}}$	$10^{10}~{\rm K~km~s}^{-1}~{\rm pc}^2$	$10^{10}{\rm Kkms^{-1}pc^2}$	$\rm Jy~km~s^{-1}$	$\rm Jy~km~s^{-1}$	$_{10^8~M_{\odot}}$	$^{10^6M_{\odot}}$	$\times 10^{-5}$	$\times 10^{-5}$		
(3) (4)	(4)		(5)	(9)	(7)	(8)	(6)	(10)	(11)	(12)	(13)	(14)	(15)
.5 9.2 ± 0.9	.2 ± 0.9		6.1 ± 0.6	1.48 ± 0.16	4.88 ± 0.63	1.9 ± 0.2	3.1 ± 0.4	32.3 ± 1.1	18.4 ± 1.9	4.3 ± 2.0	5.6 ± 2.7	0.09	z
$80 16.0 \pm 0.4$	3.0 ± 0.4		3.6 ± 0.1	0.04 ± 0.01	1	0.9 ± 0.1	ı	ı	0.5 ± 0.1	ı	ı	0.99	>
$20 10.6 \pm 1.6$	0.6 ± 1.6		2.5 ± 0.4	0.20 ± 0.03	0.39 ± 0.06	2.1 ± 0.3	2.0 ± 0.3	4.7 ± 0.7	2.5 ± 0.4	4.0 ± 2.0	9.5 ± 4.8	0.98	×
33.0 ± 1.5	3.0 ± 1.5		10.1 ± 0.5	0.27 ± 0.05	1.16 ± 0.22	2.0 ± 0.4	4.2 ± 0.8	6.6 ± 0.5	3.4 ± 0.7	3.9 ± 2.0	4.3 ± 2.3	0.74	×
1 4.2 ± 1.3	$.2 \pm 1.3$		3.6 ± 1.1	1.41 ± 0.26	4.15 ± 0.52	1.1 ± 0.2	1.6 ± 0.2	64.6 ± 20.1	17.6 ± 3.2	2.1 ± 1.2	6.2 ± 3.2	ı	Z
1 49.6 ± 3.8	9.6 ± 3.8		20.8 ± 1.6	< 8.83	ı	< 2.2	I	59.8 ± 4.6	< 110.2	< 13.9	I	0.29	7
↑ 3.7 ± 0.1	0.7 ± 0.1		2.9 ± 0.1	0.75 ± 0.12	2.36 ± 0.25	1.8 ± 0.3	2.8 ± 0.3	7.12 ± 0.02	9.4 ± 1.6	9.9 ± 4.9	5.8 ± 2.9	0.02	Z
$11 26.9 \pm 0.6$	9.9 ± 0.6		6.3 ± 0.1	0.59 ± 0.09	4.03 ± 0.06	3.9 ± 0.6	13.2 ± 0.2	8.7 ± 0.4	7.3 ± 1.1	6.4 ± 3.1	2.7 ± 1.3	0.98	¥
22 ± 2 0.74 ± 0.03	74 ± 0.03		0.55 ± 0.02	0.12 ± 0.02	0.42 ± 0.03	1.7 ± 0.3	2.8 ± 0.2	4.60 ± 0.04	1.6 ± 0.3	2.6 ± 1.3	5.5 ± 2.7	0.12	Z
1 8.4 \pm 0.4	.4 ± 0.4		5.2 ± 0.2	< 1.06	4.77 ± 0.60	< 0.7	1.6 ± 0.2	38.4 ± 1.8	< 13.2	< 2.6	< 4.1	I	Z
1 9.5 ± 0.7	1.5 ± 0.7		8.0 ± 0.8	1.39 ± 0.31	5.62 ± 0.62	0.9 ± 0.2	1.8 ± 0.2	22.9 ± 1.7	17.3 ± 3.9	5.7 ± 2.9	4.5 ± 2.4	I	Z
$20 10.2 \pm 1.0$	0.2 ± 1.0		5.0 ± 0.5	0.39 ± 0.08	1	2.3 ± 0.5	1	7.88 ± 0.04	4.8 ± 1.0	4.6 ± 2.4	I	0.18	z
32.5 ± 4.5 2.4 ± 0.1	$.4 \pm 0.1$		2.1 ± 0.1	0.69 ± 0.02	1.16 ± 0.01	16.0 ± 0.5	13.2 ± 0.1	8.7 ± 0.2	8.7 ± 0.3	7.5 ± 3.5	11.0 ± 5.1	I	Z
5.3 ± 0.3 17.8 ± 1.7	7.8 ± 1.7		5.3 ± 0.5	0.55 ± 0.08	ı	0.8 ± 0.1	I	14.5 ± 1.4	6.8 ± 1.0	3.6 ± 1.8	I	0.88	¥
20^{\dagger} 5.4 ± 0.3	$.4 \pm 0.3$		4.3 ± 0.2	0.53 ± 0.17	ı	2.8 ± 0.9	ı	7.9 ± 0.4	6.6 ± 2.1	6.3 ± 3.5	I	ı	Z
1 8.1 ± 0.4	0.1 ± 0.4		6.0 ± 0.3	1.30 ± 0.33	I	0.8 ± 0.2	Ι	15.2 ± 0.7	16.2 ± 4.1	8.1 ± 4.3	I	0.01	z
3.3 ± 0.2	3 ± 0.2		2.4 ± 0.1	< 0.95	ı	< 0.7	ı	23.9 ± 1.4	< 11.9	< 3.8	ı	1	z
1 4.6 ± 0.2	0.0 ± 0.2		3.3 ± 0.2	0.78 ± 0.22	ı	0.7 ± 0.2	ı	21.5 ± 1.1	9.7 ± 2.8	3.4 ± 1.9	I	I	z
1 4.6 ± 0.2	.6 ± 0	.2	3.3 ± 0.2	< 0.77	I	< 0.7	Ι	21.5 ± 1.1	< 9.7	< 3.4	I	ı	z
1 7.6 ± 0.3	.6 ± 0	3	6.6 ± 0.2	1.13 ± 0.32	5.23 ± 1.63	0.7 ± 0.2	1.6 ± 0.5	26.9 ± 1.0	14.1 ± 4.0	4.0 ± 2.2	4.0 ± 2.5	1	Z

 $_{\text{vor}-1}$ - ID; 2 - Spectroscopic redshift; 3 - Gravitational magnification factor; 4 - Total infrared luminosity integrated within 8 - 1000 μ m. This value is due to star formation only (i.e., corrected for torus emission) for SMGs ('V' in column 15); while it represents the SF+AGN emission for QSOs ('Y' in column 15); 5 - Far-infrared luminosity integrated within 40 - 400 μ m. This value is due to star formation only (i.e., corrected for torus emission) for SMGs ('N' in column 15), while it represents the SF+AGN emission for QSOs Atomic carbon abundances computed assuming $M_{\rm gas}({\rm CO}, \alpha_{\rm CO}=0.8~M_{\odot}/({\rm K~km~s^{-1}~pc^2}), r_{31}=0.52)$ and removing the 1.36× contribution of helium; 14 - Fraction infrared AGN emission: $L_{\rm AGN+SF}=L_{\rm IR}/(1-f_{\rm AGN})$; 15 - Quasar activity: Y(es)/N(o). ('Y' in column 15); 6, 7 - Galaxy-integrated $L'_{[CI]^3P_1-3P_0}$ and $L'_{CO(3-2)}$; 8, 9 - Velocity-integrated $[CI](^3P_1-^3P_0)$ and CO((3-2) fluxes; 10 - Dust mass; 11 - Mass of [CI] $(\text{from } L'_{[\text{CI}]^3}P_{1-3}P_0$ assuming $T_{\text{ex}}=30\ \text{K});\ 1\dot{2}$ - Atomic carbon abundances computed assuming $M_{\text{gas}}(\text{dust},\ \delta_{\text{GDR}}=30)$ and removing the $1.36\times$ contribution of helium; 13 -

Valentino et al.

Upper limits are at 3σ .

All values have been corrected for gravitational magnification.

†: From (Alaghband-Zadeh et al. 2013).

 ‡ : This source is unresolved at 850 μ m, but two components are evident in the H α and CO (4 – 3) maps. The photometry refers to the unresolved source.

SMMJ14011+0252, SMMJ16359+6612: Magnelli et al. (2012); APM08279+5255, RXJ0911+0551, F10214, Cloverleaf, PSSJ232+1944: Stacey et al. (2018); SMMJ123549+6215: W11, Kirkpatrick et al. (2012), Ivison et al. (2011); BRI1335-0417: Guilloteau et al. (1997), Carilli et al. (1999), W11, Wagg et al. (2014); SMMJ163650+4057, SMMJ163658+4105: Kovács et al. (2006), Tacconi et al. (2006), Efstathiou & Siebenmorgen (2009), W11; MMI8423+5938: Lestrade et al. (2010), Catalano et al. (2014); McKean et al. (2011); SMMJ213511-0102: Ivison et al. (2010), Swinbank et al. (2010); ID141: Cox et al. (2011); SXDF7, SXDF4a+b: Ivison et al. (2007), Alaghband-Zadeh et al. (2012, 2013); SA22.96: Menéndez-Delmestre et al. (2009), Alaghband-Zadeh et al. (2012, 2013). Cols 1-3, 8, 9, 15: Walter et al. (2011, W11), Alaghband-Zadeh et al. (2013, AZ13), and references therein; Cols 4, 5 (photometry):

Table 6. SPT sub-millimeter galaxies at $z \sim 4$.

$f_{ m AGN}$	(15)	ı	0.16	ı	ı	ı	ı	I	ı	0.62	ı	ı	0.13	1
$\frac{[C I]}{[H_2]}_{CO}$ $\times 10^{-5}$	(14)	12.9 ± 6.6	ı	I	< 3.7	12.3 ± 6.6	< 15.2	14.4 ± 7.9	ı	ı	12.5 ± 6.8	< 6.7	18.7 ± 10.4	10.5 ± 6.1
$\frac{[\text{C I}]}{[\text{H2}]}_{\text{dust}}$ $\times 10^{-5}$	(13)	4.3 ± 2.2	2.8 ± 1.5	< 4.2	< 2.7	6.1 ± 3.2	< 4.6	5.5 ± 3.0	1.6 ± 0.8	1.4 ± 0.7	6.6 ± 3.4	< 2.0	7.8 ± 4.2	4.6 ± 2.5
$M_{\rm [CI]}$ $10^6~M_{\odot}$	(12)	6.6 ± 1.3	7.1 ± 1.6	< 15.1	< 6.2	3.5 ± 0.9	< 9.0	38.5 ± 11.1	7.1 ± 1.3	10.6 ± 2.5	5.6 ± 1.4	> 8.6	21.6 ± 5.6	11.9 ± 3.5
$M_{ m dust}$ $10^8~M_{\odot}$	(11)	11.6 ± 0.1	19.0 ± 2.0	27.3 ± 2.0	17.0 ± 0.9	4.4 ± 0.1	14.7 ± 0.7	52.8 ± 2.1	33.3 ± 0.8	57.4 ± 1.3	6.4 ± 0.1	32.0 ± 0.8	20.9 ± 1.5	19.5 ± 0.5
$I_{\text{CO}(2-1)}$ Jy km s ⁻¹	(10)	1.7 ± 0.1	ı	I	1.8 ± 0.2	1.3 ± 0.1	0.9 ± 0.1	1.1 ± 0.1	I	ı	1.6 ± 0.2	0.8 ± 0.1	0.9 ± 0.2	1.2 ± 0.2
$I_{\text{[C I]}^3 P_1 - ^3 P_0}$ Jy km s ⁻¹	(6)	3.4 ± 0.7	2.4 ± 0.5	$1.8 \pm 0.8^{\dagger}$	< 1.0	2.5 ± 0.6	$1.8 \pm 0.7^{\dagger}$	2.4 ± 0.7	2.9 ± 0.5	3.2 ± 0.8	3.1 ± 0.8	$0.8 \pm 0.3^{\dagger}$	2.7 ± 0.7	2.0 ± 0.6
$L'_{\rm CO(2-1)}$ $10^{10} { m K km s^{-1} pc^2}$	(8)	1.22 ± 0.09	ı	ı	3.95 ± 0.44	0.68 ± 0.06	1.40 ± 0.21	6.37 ± 0.46	ı	1	1.06 ± 0.17	3.08 ± 0.25	2.74 ± 0.46	2.70 ± 0.54
$L'_{[CI]^3}P_1 - 3P_0$ $10^{10} \mathrm{Kkms^{-1}pc^2}$	(7)	0.53 ± 0.11	0.57 ± 0.13	< 1.21	< 0.50	0.28 ± 0.07	< 0.72	3.09 ± 0.89	0.57 ± 0.11	0.85 ± 0.20	0.45 ± 0.11	< 0.69	1.73 ± 0.45	0.95 ± 0.28
$L_{ m FIR}$ $_{10^{12}L_{\odot}}$	(9)	1.2 ± 0.1	4.9 ± 0.2	6.9 ± 0.2	15.3 ± 0.7	2.4 ± 0.1	3.9 ± 0.4	9.8 ± 0.5	3.0 ± 0.1	5.7 ± 0.5	1.51 ± 0.02	7.7 ± 0.2	5.9 ± 0.2	5.9 ± 0.9
$L_{ m IR}$	(2)	1.5 ± 0.1	10.4 ± 0.5	8.8 ± 0.2	36.0 ± 1.7	3.0 ± 0.1	7.2 ± 0.6	18.0 ± 1.0	3.5 ± 0.1	7.6 ± 0.7	1.80 ± 0.03	16.8 ± 0.4	11.4 ± 0.4	7.5 ± 1.1
M_{\star} $10^{10}~M_{\odot}$	(4)	1	I	I	ı	I	I	Ι	ı	I	I	I	$8.0^{+19.0}_{-6.0}$	$^{2.0}^{+1.8}_{-0.9}$
μgrav	(3)	23.9 ± 0.5	14.1 ± 0.5	5.7 ± 0.4	8.0 ± 0.5	32.7 ± 2.7	12.7 ± 1.0	3.6 ± 0.3	13.2 ± 0.5	10.0 ± 0.6	27.8 ± 1.8	5.7 ± 0.5	6.7 ± 0.4	6.6 ± 0.4
zspec	(5)	4.233	3.959	3.596	4.296	4.225	4.477	4.799	3.369	3.399	4.436	4.768	4.567	3.760
Ð	(1)	SPT0113-46	SPT0125-50	SPT0300-46	SPT0345-47	SPT0418-47	SPT0441-46	SPT0459-59	SPT0529-54	SPT0532-50	SPT2103-60	SPT2132-58	SPT2146-55	SPT2147-50

Nore—I - ID; 2 - Spectroscopic redshift; 3 - Gravitational magnification factor; 4 - Stellar mass from Ma et al. (2015). We did not correct it for the minimal differences in the choice of IMF (Chabrier (2003) vs Kroupa (2001)) and stellar population models (Bruzual & Charlot (2003) vs Maraston (2005), see Section 6.1 in Ma et al. 2015); 5 - Total infrared luminosity integrated within 8 - 1000 μ m due to star formation (i.e., corrected for torus emission); 6 - Far-infrared luminosity integrated within 40 - 400 μ m due to CO(2-1) fluxes; 11 - Dust mass; 12 - Mass of [CI] (from $L'_{[C1]^3P_1-3P_0}$ assuming $T_{ex}=30$ K); 13 - Atomic carbon abundances computed assuming $M_{gas}(dust,\delta_{GDR}=30)$ and star formation (i.e., corrected for torus emission); 7, 8 - Galaxy-integrated $L'_{[C1]^3P_1-3P_0}$ and $L'_{CO(2-1)}$; 9 - Velocity-integrated $[C1](^3P_1-^3P_0)$ fluxes; 10 - Velocity-integrated removing the 1.36× contribution of helium; 14 - Atomic carbon abundances computed assuming $M_{\rm gas}({\rm CO},\,\alpha_{\rm CO}=0.8\,M_{\odot}/({\rm K~km~s^{-1}~pc^2}),\,r_{21}=0.84)$ and removing the 1.36× contribution of helium; 15 - Fraction infrared AGN emission: $L_{\rm AGN+SF} = L_{\rm IR}/(1-f_{\rm AGN})$.

Upper limits are at $3\sigma.$ All values have been corrected for gravitational magnification.

 † : We report the nominal flux measurements presented in Bothwell et al. (2017), but we adopt the 3σ upper limits for the analysis.

References: Cols 1-3, 9: Bothwell et al. (2017); Col 4: Ma et al. (2015); Cols 5, 6 (photometry): Weiß et al. (2013); Col 10: Aravena et al. (2016).